Mechanism of Ethylene Oxychlorination on Ceria

Journal Article

Author(s):
Scharfe, Matthias; Capdevila-Cortada, Marçal; Kondratenko, Vita A.; Kondratenko, Evgenii V.; Colussi, Sara; Trovarelli, Alessandro; López, Núria; Pérez-Ramírez, Javier

Mechanism of Ethylene Oxychlorination on Ceria

Matthias Scharfe[†], Marçal Capdevila-Cortada[‡], Vita A. Kondratenko[§], Evgenii V. Kondratenko[§],

Sara Colussi[‖], Alessandro Trovarelli[‖], Núria López[‡,*], and Javier Pérez-Ramírez[†,*]

[†] Institute for Chemical and Bioengineering, Department of Chemistry and Applied Biosciences,

ETH Zurich, Vladimir-Prelog-Weg 1, 8093 Zurich, Switzerland.

[‡] Institute of Chemical Research of Catalonia (ICIQ), The Barcelona Institute of Science and

Technology, Av. Països Catalans 16, 43007 Tarragona, Spain.

[§] Leibniz-Institut für Katalyse e. V., Albert-Einstein-Straße 29a, 18059 Rostock, Germany.

[‖] Dipartimento Politecnico, Università di Udine, via del Cotonificio 108, 33100 Udine, Italy.

ABSTRACT

Ethylene oxychlorination on CeO_2 provides ethylene dichloride (EDC) and the desired vinyl chloride (VCM) in a single operation in contrast to the traditional process that requires two separated units. The origin of this outstanding performance is unclear and the mechanism has not been discussed in detail. In the present work, we combine density functional theory (DFT) with steady state experiments and temporal analysis of products (TAP) to close this gap. The catalyst surface is found to contain CeOCl, while the bulk phase is CeO_2, regardless of the starting phase $CeCl_3$, CeOCl, or CeO_2. Catalysis by different nanostructures highlights that $CeO_2(111)$ surfaces are more active than (100) due to the poisoning of the latter, while the selectivities are comparable. In any case, the degree of oxygen vacancy formation and its replenishment by Cl species leads to increased selectivity to chlorinated products, and decreased selectivity to carbon oxides. DFT and TAP studies reveal that the most likely pathway of vinyl chloride (VCM) formation takes place by a cascade reaction. First, ethylene dichloride (EDC) appears and then HCl is extruded in a concerted step to lead to VCM. Such steps are a key characteristic of ceria. Other paths leading to minor products such as 1,2-dichloroethene (DCE) are found possible starting from both VCM or EDC. Oxidation products like CO are formed by combustion of chlorinated species, whereas CO_2 can either stem from further oxidation of CO or directly from ethylene. In summary, our work points out a rich complex behavior of the chemistry of chlorinated compounds on the oxide surface indicating that concerted steps and cascade reactions are possible for these materials.

KEYWORDS: ethylene oxychlorination, mechanism, CeO_2, oxychloride, oxygen vacancies, density functional theory, temporal analysis of products

1. INTRODUCTION

Polyvinyl chloride (PVC) constituted a 53 billion USD market in 2015, growing with a compound annual growth rate of 5.3%.[1] Its corresponding monomer, vinyl chloride (commonly denoted as VCM), is either produced through hydrochlorination of acetylene,[2–4] through energy-intensive thermal dehydrochlorination of 1,2-dichloroethane (known as ethylene dichloride, EDC) with a low yield of 49-58%.[5] EDC is in turn, either formed by Cl_2 addition to ethylene or by ethylene oxychlorination. The latter enables recycling of HCl from the dehydrochlorination step in the balanced VCM process.[5–7] To date, the catalyst in ethylene oxychlorination comprises cupric chloride ($CuCl_2$) as the active phase, impregnated on a porous support such as alumina, and promoted by numerous alkali, alkaline earth, and rare earth metals to reduce the copper loss and/or improve the activity and selectivity.[8–11] However, while achieving an EDC selectivity of 99%, issues surrounding active phase volatilization or particle stickiness are not yet fully resolved.[12] Nevertheless, the mechanism of ethylene oxychlorination on $CuCl_2$ based catalysts was unveiled by numerous *in-situ* and *operando* spectroscopy studies.[13–17] Briefly, the process encompasses a three-step redox mechanism: (*i*) chlorination of ethylene by reduction of $CuCl_2$ to CuCl, (*ii*) formation of a cupric oxychloride by oxidation of CuCl, and finally (*iii*) closure of the catalytic cycle though re-chlorination of the oxychloride with HCl and water elimination.[6,9,10,13,14,16,18–26]

Recently, the great potential of CeO_2 in ethylene oxychlorination was uncovered, revealing a stable bifunctional character and enabling direct VCM and EDC production with single-step yields up to 25%.[27] Some of us put forward that this VCM formation is attributed to the material acidity, correlating with the EDC dehydrochlorination performance of CeO_2 and that higher chlorination leads to higher EDC selectivity and suppressed oxidation routes.[27] Alternative

materials, also based on rare earths such as EuOCl, rendered less active but highly selective towards VCM (75%) and evidenced the selectivity-acidity link.[28] However, a previous study aiming to shed light on the complex ethylene oxychlorination reaction network on oxide or oxychloride based materials, used the Density Functional Theory (DFT) on RuO_2 as a model catalyst due to the simplest electronic structure.[29] RuO_2 is a poor oxychlorination catalyst as it mostly forms CO_2 and only small amounts of EDC and VCM during reaction. Nevertheless, investigation of 34 elementary steps over the relatively simple surface revealed that oxidation processes are thermodynamically favored, whereas chlorination processes are kinetically controlled.[29] In addition, the surface chlorine uptake, *i.e.,* the chlorine coverage, is a key factor determining the selectivity of RuO_2. Only high chlorine coverage allows VCM displacement by C_2H_4 thus preventing the formation of VCM derived products, however at the same time it destabilizes C_2H_4Cl intermediates, favoring the formation of EDC instead of VCM.[29]

In this study, we investigate the mechanism of ethylene oxychlorination over CeO_2 as it rendered the most active in a broad range of conditions and exhibited a strong impact of the feed concentrations of HCl and O_2 on the activity and selectivity to chlorinated products.[27,28] In addition, CeO_2 shows a correlation between dehydrochlorination performance and surface acidity, of which the exact nature is yet unknown. Even though CeO_2 has a more complex electronic structure than RuO_2, the computational set-up based on DFT+U has proven reasonably accurate.[30–36] As our experiments reveal that the active phase in oxychlorination is actually an oxychloride, previous studies of the mechanism of oxychlorination on RuO_2 and chlorination of RuO_2 and CeO_2 in the related HCl oxidation potentially allow knowledge transfer to this work or accompany our findings.[29,32,37–40] We prove and complement the theoretical insight by DFT with

advanced transient kinetic studies, uncovering the reaction pathways that lead to chlorine-containing hydrocarbons and suggesting the routes for combustion.

2. MATERIALS AND METHODS

2.1. Catalyst preparation. Commercial CeO_2 (Sigma–Aldrich, 99.5%) was calcined at 873 K or 1023 K in static air using a heating rate of 5 K min^{-1} and an isothermal step of 5 h prior to its use in the catalytic studies. $CeCl_3$ (ABCR, 99.9%) was calcined at 423 K in static air using a heating rate of 5 K min^{-1} and an isothermal step of 5 h in order to desorb any adsorbed species, while not transforming it to CeO_2. The catalysts are hereafter denoted as $CeCl_3/CeO_2$-x(-py)(-Ez), where x is the calcination temperature in K, y the pre-reduction temperature in K if applied, and Ez indicates a used material in ethylene oxychlorination at a reaction temperature of z in K. CeOCl was prepared by calcination at 1023 K, following the method reported by Farra *et al*.[41] CeO_2 nanocubes (CeO_2-NC) were hydrothermally synthesized, optimizing procedures reported elsewhere.[42–44] Briefly, 5.21 g of $Ce(NO_3)_3 \cdot 6H_2O$ was dissolved in 30 ml of distilled water to which 210 ml of 6.9 M NaOH solution was added dropwise under vigorous stirring. After precipitation, the suspension was transferred into a Teflon-lined cylinder, sealed in a stainless-steel autoclave, and kept at 453 K for 24 h. Subsequently, the suspension was cooled to room temperature, centrifuged, and washed three times with water and ethanol, before the product was dried overnight at 333 K and calcined in static air at 773 K for 3 h.

2.2. Catalyst characterization. N_2 sorption at 77 K was measured in a Quantachrome Quadrasorb-SI analyzer. Prior to the measurements, the samples were outgassed to 50 mbar at 573 K for 12 h. The Brunauer-Emmett-Teller (BET) method was applied to calculate the total surface area, S_{BET}, in m^2 g^{-1}.[45] Oxygen storage capacity (OSC) measurements were performed by

thermogravimetric analysis (TGA) on a TA Instruments Q500 apparatus. The sample (30 mg) was loaded on a platinum pan, pre-treated in N_2 (60 cm^3 STP min^{-1}) at 573 K for 1 h, ramped up to 673 K and equilibrated for 15 min. Thereafter, a flow with 4.5 vol.% H_2 in N_2 (60 cm^3 STP min^{-1}) was introduced and kept for 2 h (1st OSC measurement) before purging with N_2 for 5 min and re-oxidizing the sample with air (60 cm^3 STP min^{-1}) for 1 h. After a second purge in N_2 for 5 min, a second OSC measurement was performed under identical conditions. Then, two more OSC measurements were performed, following the same procedure in order to ensure that no chlorine removal would impair the measured OSC. The chlorine content in the used samples was estimated by four independent X-ray fluorescence (XRF) spectroscopy measurements using an Orbis PC Micro-EDXRF analyzer with a Rh source (35 kV, 500 µA) and a silicon drift detector. A chlorine background signal was determined in four fresh CeO_2-873 at 0.3 at.% and subtracted from all averaged measurements. Powder X-ray diffraction (XRD) was measured using a PANalytical X'Pert PRO-MPD diffractometer and Cu-Kα radiation ($\lambda = 0.15418$ nm). The data was recorded in the 10-70° 2θ range with an angular step size of 0.017° and a continuing time of 0.26 s per step.

2.3. Catalytic testing. The steady-state oxychlorination of ethylene was investigated at ambient pressure in a continuous-flow fixed-bed reactor (Scheme S1). The set-up consists of (*i*) mass flow controllers to feed C_2H_4 (PanGas, 3.5), HCl (Air Liquide, 2.8, anhydrous), O_2 (Messer, 19.96% in He), He (PanGas, 5.0) as a carrier gas, and Ar (PanGas, 5.0) as an internal standard, (*ii*) a syringe pump (Nexus 6000, Chemyx) to feed EDC (Fluka, 99.5%), (*iii*) a vaporizer operated at 403 K accommodating a quartz T-connector filled with glass beads to vaporize EDC, (*iv*) an electrically heated oven hosting a quartz micro-reactor equipped with a K-type thermocouple whose tip reaches the center of the catalyst bed, (*v*) downstream heat

tracing to avoid any condensation of the reactants and products, and (*vi*) a gas chromatograph coupled to a mass spectrometer (GC-MS) for on-line analysis. The effluent stream was neutralized by passing it through an impinging bottle containing an aqueous NaOH solution (1 M). The catalyst (W_{cat} = 0.5 g, particle size d_p = 0.4-0.6 mm) was loaded in the micro-reactor (10 mm inner diameter) and pretreated in He at 473 K for 30 min. Thereafter, a total flow (F_T) of 100 cm^3 STP min^{-1} with a composition of C_2H_4:HCl:O_2:Ar:He = 3:1-6:1-6:3:83.2-90, where Ar acted as internal standard and He was used as carrier gas, was fed to the reactor at a bed temperature (*T*) of 423-773 K and pressure (P) of 1 bar. Note that relatively low feed concentrations were selected to prevent corrosion, enable safe handling, and minimize the formation of hot spots in the catalyst bed due to the high reaction exothermicity. The standard conditions of C_2H_4:HCl:O_2:He = 3:4.8:3:89.2 were chosen based on the literature.[12,27] Prior to the analysis of the reaction mixtures, the catalysts were equilibrated for at least 1 h under each condition. The gas composition at the reactor outlet, containing reactants (C_2H_4, O_2, HCl) and products (EDC, VCM, DCE, EC, CO, CO_2), was determined online using a gas chromatograph equipped with a GS-CarbonPLOT column coupled to a mass spectrometer (Agilent GC 7890B, Agilent MSD 5977A) with a triple-axis detector and an electron multiplier. A representative chromatogram is depicted as an inset in Scheme S1. In the HCl oxidation tests, the Cl_2 production was quantified by offline iodometric titration (using a Mettler Toledo G20 Compact Titrator) of triiodide, formed by purging the Cl_2 containing reactor outlet through an aqueous KI (Sigma-Aldrich, 99.5%) solution (0.1 M), with 0.01 M sodium thiosulfate solution (Sigma-Aldrich, 99.99%). The conversion of HCl in HCl oxidation experiments, X(HCl), was calculated using Eq. 1,

$$X(\text{HCl}) = \frac{2x_{Cl_2,\text{outlet}}}{x_{\text{HCl,inlet}}} \cdot 100\% \qquad \text{(Eq. 1)}$$

where $x_{HCl,inlet}$ and $x_{Cl_2,outlet}$ denote the volumetric concentration of HCl and Cl_2 at the reactor inlet and outlet, respectively. The conversion of ethylene in ethylene oxychlorination experiments, $X(C_2H_4)$, was calculated according to Eq. 2,

$$X(C_2H_4) = \frac{x_{C_2H_4,inlet} - x_{C_2H_4,outlet}}{x_{C_2H_4,inlet}} \cdot 100\%$$ (Eq. 2)

where $x_{C_2H_4,inlet}$ and $x_{C_2H_4,outlet}$ denote the volumetric concentration of ethylene at the reactor inlet and outlet, respectively. The selectivity of a reaction product j, $S(j)$, was calculated according to Eq. 3,

$$S(j) = \frac{x_j / n_j}{\sum x_j / n_j} \cdot 100\%$$ (Eq. 3)

where x_j and n_j denote the volumetric concentrations of product j at the reactor outlet and the corresponding stoichiometric factor with respect to the number of carbon atoms, respectively ($e.g.$, $C_2H_4 + 2O_2 \rightarrow 2CO + 2H_2O$, $n_{CO} = 2$).

The carbon mass balance error ε_C was determined using Eq. 7,

$$\varepsilon_C = \left| \frac{x_{C_2H_4,j,inlet} - \sum x_{C_2H_4,j,outlet} / n_{C_2H_4,j,outlet}}{x_{C_2H_4,j,inlet}} \right| \cdot 100\%$$ (Eq. 4)

where $x_{C_2H_4,j}$ and $n_{C_2H_4,j}$ denote the concentration of ethylene or product j at the reactor inlet or outlet and the corresponding stoichiometric factor with respect to the number of carbon atoms, respectively. Each catalytic data point reported is an average of at least three measurements. The carbon mass balance in all catalytic tests closed at 96% or higher. After the tests, the catalyst bed was quenched to room temperature in He flow.

2.4. Temporal analysis of products. Overall reaction pathways of product formation in ethylene oxychlorination over an equilibrated catalyst sample (CeO$_2$-873-E673) were studied by temporal analysis of products (TAP), a transient pulse technique with a time resolution of approximately 100 μs.[46–48] The used TAP-2 system is equipped with an in-house developed quartz-tube fixed-bed reactor (d_{in} = 6 mm, L = 40 mm) in which the catalyst (W_{cat} = 65 mg, particle size d_p = 0.3-0.5 mm) was packed between two layers of quartz of the same particle size within the isothermal zone of the reactor. Then, the reactor was evacuated stepwise to 10^{-5} Pa. The pulse experiments were carried out at 673, 723, and 773 K using C$_2$H$_4$:Ne = 1:1, C$_2$H$_4$:O$_2$:Ne = 1:1:1, HCl:Ar = 1:1, Cl$_2$:Ar = 1:1 and C$_2$H$_4$Cl$_2$:Ar = 1:6 mixtures. An overall pulse size was around 10^{16} molecules. Ne (Linde Gas, 5.0), Ar (5.0, Linde Gas), O$_2$ (Air Liquide, 4.8), C$_2$H$_4$ (Air Liquide, 3.5), EDC (Sigma-Aldrich, 99.8%), and HCl (Air Liquide, 4.5, anhydrous) were used for preparing reaction mixtures without additional purification. A quadrupole mass spectrometer (HAL RC 301 Hiden Analytical) was used for quantitative analysis of feed components and reaction products where the following AMUs were assigned for mass-spectrometric compound identification: 70 (Cl$_2$), 66 (EC), 64 (EC, EDC, VCM), 62 (EDC, VCM), 49 (EDC), 44 (CO$_2$), 36 (HCl), 32 (O$_2$), 29 (EC), 28 (EC, EDC, CO$_2$, CO, C$_2$H$_4$), 27 (EC, EDC, VCM, C$_2$H$_4$), 26 (EC, EDC, VCM, C$_2$H$_4$), 22 (Ne), 18 (H$_2$O), 2 (H$_2$O, H$_2$), 40 (Ar) and 20 (Ar, Ne). Pulses were repeated 10 times for each AMU and averaged to improve the signal-to-noise ratio.

2.5. Density functional theory. All calculations were performed with periodic boundary conditions at the density functional theory level, implemented in the Vienna *ab initio* simulation package (VASP, version 5.3.5),[49–51] using the Perdew-Burke-Ernzerhof (PBE) functional.[52] Projector-augmented wave (PAW) pseudopotentials were used to consider the inner electrons,

whereas valence electronic states were expanded in plane-waves with an energy cut-off of 500 eV.[53] In order to reduce the self-interaction error, an effective Hubbard potential (U_{eff}) of 4.5 eV was added to the Ce(4f) states.[54] Spin polarized calculations were performed when required. Van der Waals contributions were included by using the D3 dispersion correction method of Grimme *et al.*[55] The criteria for electronic and geometry optimization convergence were set to 10^{-6} eV and 0.015 eVÅ^{-1}, respectively. The lattice parameter of CeO_2 was optimized with a dense 7 x 7 x 7 Γ-centered k-point mesh and an energy cut-off of 700 eV, leading to the lattice parameter $a_{\text{calc}} = 5.492$ Å, which is in good agreement (1.5% deviation) with the experimental value of $a_{\text{exp}} = 5.411$ Å.[56] The investigated (111) surface was thereafter modeled as periodically repeated slabs using a 3 x 3 x 1 Γ-centered k-point mesh. The slabs were separated by 15 Å of vacuum space on top and consisting of 3 x 3 unit cells with three and six layers of Ce and O atoms, of which the upper two Ce- and four O-layers were allowed to relax. Chlorination of the surface was considered in the uppermost layer by replacement of O atoms with Cl atoms. The regular O-terminated CeO_2(100) surface was modeled as a 2 x2 supercell as described in the literature with the same k-point sampling and vacuum space as the (111) surface.[57] The climbing image nudged elastic band (CI-NEB) method and corresponding vibrational analysis were used to identify the transition states in the reaction network.[58,59] The structures, labeled with the same names as described in this work are freely accessible from the ioChem-BD database.[60,61] The vibrational, rotational and translational entropies of gas phase molecules were calculated using Gaussian 03W (Version 6.1),[62] employing DFT with PBE functionals, a cc-pVQZ basis set, the RMS force criterion set to 10^{-5}, and the temperature set to 673.15 K. The Gibbs free energy was calculated by taking the vibrational entropy into account, as implemented in Gaussian and described by Ochterski.[63]

3. RESULTS AND DISCUSSION

3.1. Impact of material properties. In order to choose the right model catalyst for this study, the first step was to identify which type of material is present during the reaction by correlating steady-state activity with the bulk-phase composition. Figure 1a-c depicts the conversion of ethylene and selectivity to various products in ethylene oxychlorination on $CeCl_3$, $CeOCl$, and CeO_2. The temperature was cycled from 423 K to 723 K and backwards in order to achieve strongest hysteresis behavior, as it can be expected that $CeCl_3$ transforms to the oxide in an oxygen containing atmosphere at high temperatures. The material that behaves quite differently from the rest during up- and down-cycling is $CeCl_3$, which shows first only formation of ethyl chloride before the conversion drops to almost zero until 723 K, where about 58% conversion is reached. At this temperature, the product distribution is similar to the one of $CeOCl$ and CeO_2, while the activity is about the same of $CeOCl$ and a bit higher than the one of CeO_2. However, most importantly, the cooling-part of the cycle is qualitatively the same in all three materials, suggesting a transformation of the different starting materials to one and the same phase. As $CeOCl$ and CeO_2 do not exhibit such a hysteresis behavior, it is likely that this common phase is an oxychloride, which either exists from the beginning in $CeOCl$ or forms easily and fast from CeO_2 through chlorination already at low temperatures. XRD evidences the prevalence of bulk CeO_2 in all samples after the test (Figure 1d-f), whereas elemental mapping (Figure 1g-i) shows the presence of oxygen and chlorine throughout all samples. Previous studies in HCl oxidation report that CeO_2 mainly chlorinates on the surface or only to some extent in the near-subsurface region at O_2:HCl feed ratios greater than 0.75,[32] 1,[37] or 2,[64] constituting a rather large spread.
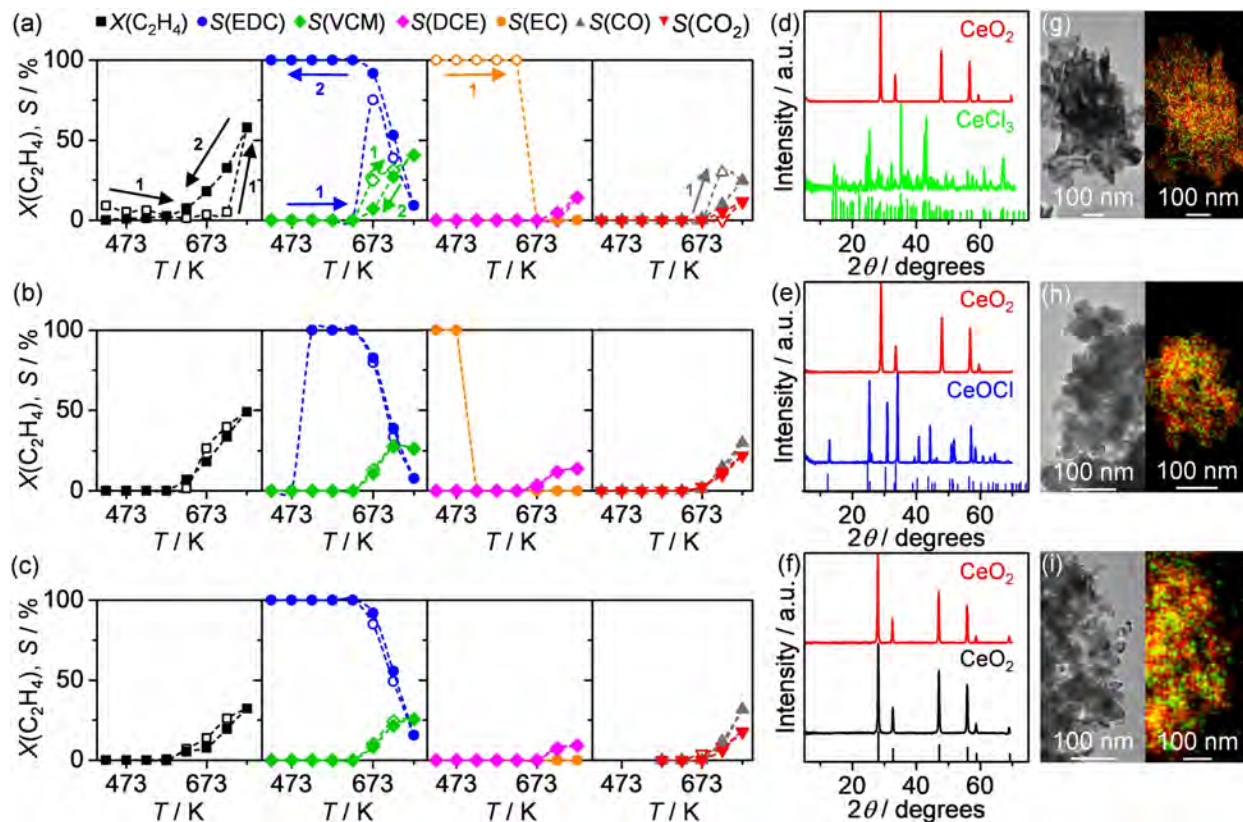
Figure 1. Ethylene conversion (X) and selectivity (S) *versus* temperature ramping up (arrow 1, open symbols) and down (arrow 2, solid symbols) over (a) $CeCl_3$-423, (b) CeOCl-1023, and (c) CeO_2-1023. Other conditions: C_2H_4:HCl:O_2 = 3:4.8:3, W_{cat} = 0.5 g, F_{tot} = 100 cm^3 STP min^{-1}, P = 1 bar. XRD patterns of fresh (bottom) (d) $CeCl_3$-423 (green), (e) CeOCl-1023 (blue), and (f) CeO_2-1023 (black) with corresponding reference patterns of $CeCl_3$ (ICDD PDF 77-0154 and 01-0149), CeOCl (ICDD PDF 73-5027) and CeO_2 (ICDD PDF 73-6318) and used catalysts (top, red) that all show only the CeO_2 phase corresponding again to (ICDD PDF 73-6318). (g-h) HRTEM images (left) and elemental maps (right, where red depicts O and green Cl, respectively) of used catalysts corresponding to (a-c).

As the used ethylene oxychlorination reaction conditions are in general closer to the ones reported in the former two publications, ceria was previously proven stable in oxychlorination of ethylene,[27] and the XRD patterns of used catalysts in Figure 1(d-f) only show the presence of the oxide phase, we estimate that the bulk material keeps the oxide nature while the catalytically active surface consists of an oxychloride. In addition, key DFT calculations show that the energy required to displace one Cl atom from the surface to a subsurface position is 3 eV, indicating that

this is an unlikely event. The used CeOCl and CeO_2 samples exhibit mostly octahedral morphologies, whereas the CeO_2 formed from $CeCl_3$ shows less developed crystals, likely due to insufficient oxygen availability during such transformation. However, this insight on the composition of the surface does not yet allow conclusions about which facet of chlorinated ceria should be the model surface for further studies. Therefore, we investigated the performance of polycrystalline ceria and CeO_2 nanocubes (CeO_2-873-E673 and CeO_2-NC-E673), exposing predominantly the (111) and (100) surface, respectively. Figure S1 shows that there are no significant differences in selectivity between the nanocubic and polycrystalline sample when comparing them at equal conversion (Figure S2 depicts the relationship of conversion and product distribution of our standard sample). The only difference is the slightly decreased combustion in favor of higher selectivity to chlorinated hydrocarbons of CeO_2-NC-E673, which can be explained by easier chlorination of the (100) surface compared to the (111) surface, evidenced by a much higher net (Table S1) and per surface area (Figure S1) chlorine uptake. The latter is likely also a reason for the reduced activity, together with the lower surface area of the used nanocubes (19 m^2 g^{-1} *versus* 39 m^2 g^{-1}). Studies in HCl oxidation and trimethoxybenzene oxyhalogenation have previously shown similar results where nanooctahedra exhibited a higher activity per surface area compared to nanocubes.[64,65] However, the chlorine uptake was therein reported higher in the octahedrons than in the cubes, contrasting our findings which is most likely linked to different conditions and absence of ethylene.[64] Furthermore, whilst the stability of the two different CeO_2 morphologies under reaction conditions is comparable, as evidenced by HRTEM analysis of fresh and used samples (Figure S1b-e), the (111) surface is generally more stable from a thermodynamic point of view.[66]
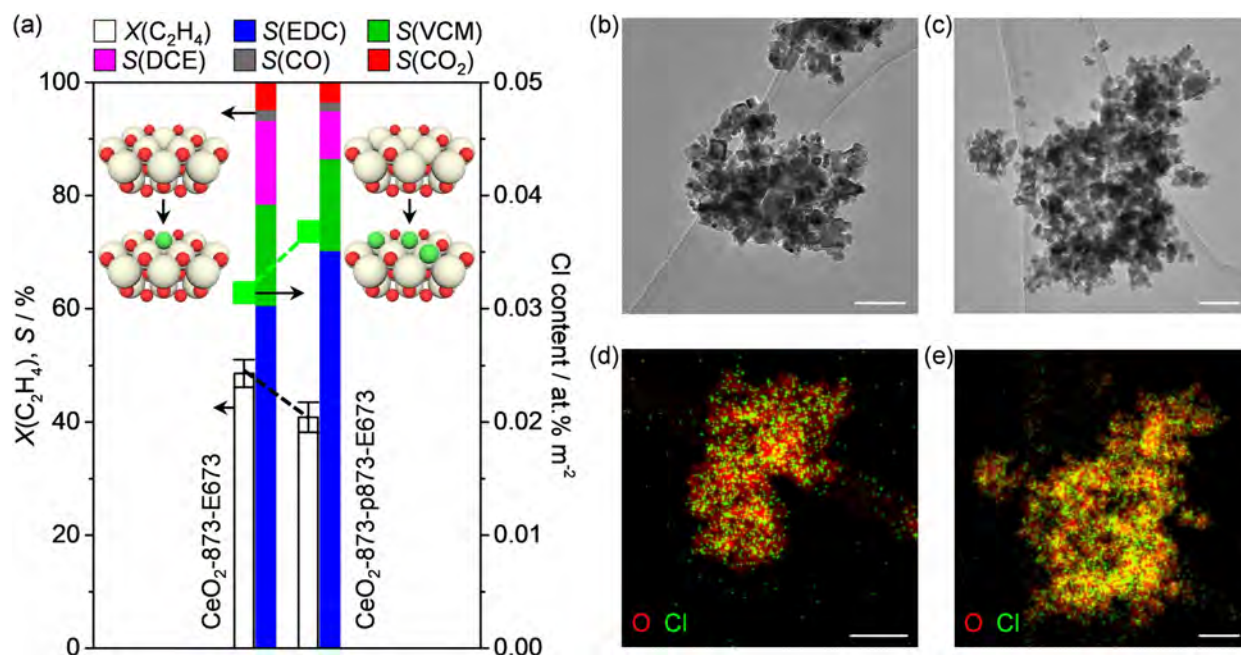
Figure 2. (a) Conversion and selectivity of ethylene oxychlorination at 673 K on CeO_2-873 without pre-treatment and with a pre-reduction in 5 vol% H_2 at 873 K for 2 h. The right axis indicates the chlorine content per surface area of the used catalysts (see also Table S1). Other conditions: C_2H_4:HCl:O_2 = 3:4.8:3, W_{cat} = 0.5 g, F_{tot} = 100 cm³ STP min⁻¹, P = 1 bar, time-on-stream 2 h. The insets schematically depict the principle of chlorination where the top part shows CeO_2 with a low or high amount of vacancies formed by pre-reduction, which leads to low or high chlorination (yellow Ce, red O, green Cl). (b,c) HRTEM images and (d,e) elemental mapping of CeO_2-873-E673 and CeO_2-873-p873-E673. The scale bars in the micrographs represent 100 nm.

However, as the effect of oxygen vacancies and their possible chlorination is yet unclear, we conducted experiments with *in-situ* pre-reduced CeO_2, in order to create vacancies before exposing the material to our reaction conditions. These vacancies can be filled by oxygen or chlorine during the reaction as depicted in the schemes in Figure 2a (see Table S1 for surface areas and chlorine contents), while chlorination is preferred by 0.89 eV (*vide infra*). In turn, the higher degree of chlorination leads to less activity, less combustion, and improved EDC selectivity of CeO_2-873-p873-E673 with respect to the reference sample CeO_2-873-E673 (Figure 2a). Even though the structure is preserved in both cases (HRTEM images of used catalysts show no significant differences and octahedrons are still clearly visible), elemental

14

mapping also evidences much more chlorine in CeO_2-873-p873-E673 than in CeO_2-873-E673 (Figure 2b-e), confirming the XRF measurements. Therefore, vacancies are at least partly healed by incorporation of chlorine rather than oxygen during reaction conditions, thus creating a surface oxychloride structure and constituting an important factor determining the selectivity. The number of vacancies that forms under reaction conditions was determined by measurement of the oxygen storage capacity (OSC), a technique widely applied in the literature.[66]

In general, an increase of the OSC of used materials compared to fresh CeO_2 (50 µmol O_2 g^{-1} for CeO_2-873-E673 $versus$ 34 µmol O_2 g^{-1} for CeO_2-873) is observed. This increase of OSC would suggest that during reaction, the surface or bulk of CeO_2 is modified by the introduction of chlorine, which can then alter the way CeO_2 interacts with H_2/O_2 during OSC measurements. Detection of chlorine traces by XRF (0.7 at.%) in the sample even after four reduction/oxidation cycles indicates that chlorine modifies the material permanently. This is also evidenced by the OSC value which stays constant at ca. 50 µmol O_2 g^{-1} after three cycles. The literature supports the presence of non-removable chlorine in ceria, suggesting that CeOCl patches which form on the surface can grow into subsurface layers at temperatures at or above 673 K.[67,67] Furthermore, Cl was found to remain in the lattice until 1173 K under reducing conditions.[69] Interestingly, pre-reduction of CeO_2 with 5% H_2 in He at 873 K has the same effect on the OSC as the oxychlorination reaction carried out at 673 K (CeO_2-873-p873 and CeO_2-873-E673 both exhibit an OSC of exactly 50 µmol O_2 g^{-1}). Furthermore, the pre-reduced sample after reaction CeO_2-873-p873-E673 also exhibits an OSC of 53 µmol O_2 g^{-1}. This corroborates the assumption that the incorporation of non-removable chlorine in the bulk does facilitate vacancy formation in other areas of CeO_2, as also observed in a study on chlorine poisoning of Ce/Zr mixed oxide catalysts.[70] However, further investigations of these aspects would go beyond the scope of this

work. In conclusion, vacancies and chlorination are strongly linked and cannot be discussed separately. While the existence of vacancies seems important to allow a certain extent of surface chlorination which suppresses combustion and allows the reaction to take place, too many vacancies, leading to too high chlorination, are detrimental for the performance. Furthermore, even though it cannot be excluded that chlorine atoms from the surface diffuse into subsurface layers, substantial subsurface chlorine populations are unlikely as they correspond to highly endothermic processes. Taking all of the above into account, a stoichiometric $CeO_2(111)$ surface as reference and the same surface with one defect, *i.e.*, one vacancy that can be filled by one chlorine atom became the surfaces of choice for the DFT investigations.

3.2. Reaction mechanism. Initial calculations of the two model surfaces showed the existence of three distinct adsorption sites, of which the stoichiometric surface exhibits two (lattice oxygen and lattice cerium atoms) and the defective surface exhibits an oxygen vacancy in addition. HCl adsorbs dissociatively on $CeO_2(111)$, where the hydrogen proton binds to a lattice oxygen and the chlorine anion either adsorbs on top of a Ce atom ($E_{ads} = -1.40$ eV) or in an oxygen vacancy ($E_{ads} = -3.16$ eV). As the difference in adsorption energy is relatively high, it is plausible that once vacancies exist, chlorine will predominantly fill them, in accordance with high Cl activation barriers in HCl oxidation.[32] In contrast to the (111) surface, HCl adsorption on the regular O-terminated (100) surface[57] is much stronger (E_{ads}(HCl) $= -3.64$ eV and E_{ads}(2HCl) $= -6.08$ eV) and Cl evolution is very energy intensive (2.64 eV) and thus unlikely. Therefore, once HCl adsorbs on $CeO_2(100)$, Cl is very likely to stay on that surface, thus poisoning it, which explains the relative inertness of this surface. Similar to HCl adsorption on $CeO_2(111)$, even though non-dissociative, chlorinated hydrocarbons also occupy up to three adsorption sites simultaneously. While ethylene adsorbs on top of a lattice cerium, chlorinated
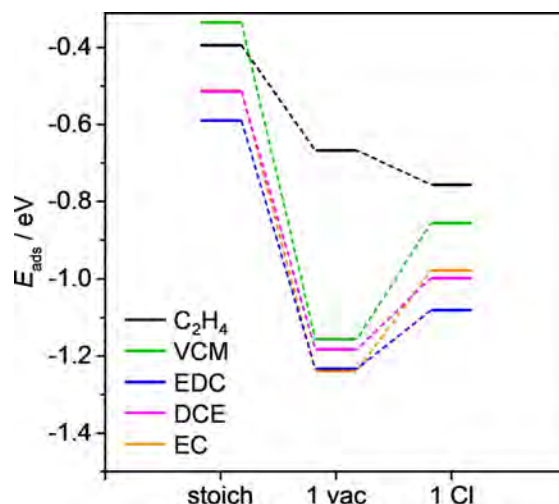
Figure 3. Adsorption energies of ethylene and chlorinated products on a stoichiometric surface, stoich, and two defect surfaces with either one oxygen vacancy, 1 vac, or one incorporated chlorine atom, 1 Cl.

hydrocarbons occupy one lattice oxygen and neighboring Ce atoms or vacancies (Figure S3, S4).

The same holds for chemisorbed intermediates, where lattice oxygen creates a bond to one C

atom and the potential chlorine ends orientate so that they occupy Ce atoms or vacancies (*vide*

infra). A comparison of the adsorption energies of ethylene and chlorinated products on a

stoichiometric, an oxygen vacant and a chlorinated surface (Figure 3, Table S2) yields that

ethylene is generally weakly adsorbed and EDC is always the most strongly adsorbed compound,

with the exception of the case with one oxygen vacancy where EC adsorbs with the same energy.

DCE exhibits a slightly weaker adsorption, similar to EC, while VCM is always the least

strongly bound product. Therefore, EDC, EC, and DCE are more like to take part in further

transformations than VCM if the barriers are reasonably low. This is very desirable, however,

VCM is only on the stoichiometric surface less strongly adsorbed than ethylene and the

adsorption energies of all products on the oxygen vacant surface are very close. The latter can be

explained by the fact that the presence of a vacancy acts as an ideal trapping site for the

chlorinated end of each molecule and therefore other contributions are less important

(Figure S4). Nevertheless, the result of this comparison is not in line with the experimentally observed selectivity (Figure 1, 2, S2) and therefore not sufficient to unravel the mechanism of ethylene oxychlorination on CeO_2.

Our previous work proposes a sequential mechanism of ethylene oxychlorination to EDC and its dehydrochlorination to VCM, as depicted in dashed black in Figure 4, which represents the starting point of a transition state investigation on a stoichiometric and defective surface. However, some elementary steps in this pathway are highly unlikely due to high barriers for the formation of EDC (stoichiometric: 1.98 eV, defective: 2.77 eV, step 3 in Table S2). In addition, step 14 rendered unfeasible as the stripping of one chlorine atom always also involves the stripping of the second chlorine atom, leading to a surface bound C_2H_3. Therefore, this pathway needs to be discarded, but an alternative consecutive mechanism could be imagined by ceria enabling concerted steps,[71] *i.e.*, the combination of individual steps into one elementary step, as depicted by solid black in Figure 4. Herein, path 1a combines the addition of one chlorine atom from a vacancy and another chlorine atom that is adsorbed on top of a cerium atom to ethylene. The following path 7a represents the simultaneous abstraction of H and Cl from EDC, directly leading to VCM. Figure 5 and Table 1 report the reaction profile along these paths.

In fact, step 1a was found to consist of two individual steps (reaction coordinate 2-6, steps 1a-1, 1a-2) with barriers of 1.16 and 0.60 eV as the chlorine addition is not fully symmetric and thus a non-surface-bound C_2H_4Cl-intermediate with only real frequencies exists. In other words, after ethylene and HCl adsorption from the gas phase, ethylene attacks the chlorine on top of a cerium atom (reaction coordinate 2-4), while in the second part, this intermediate, directly picks up the chlorine from a vacancy (left inset in Figure 5). Nevertheless, this path is still greatly favored over the two individual steps with a surface bound C_2H_4Cl intermediate, or the situation
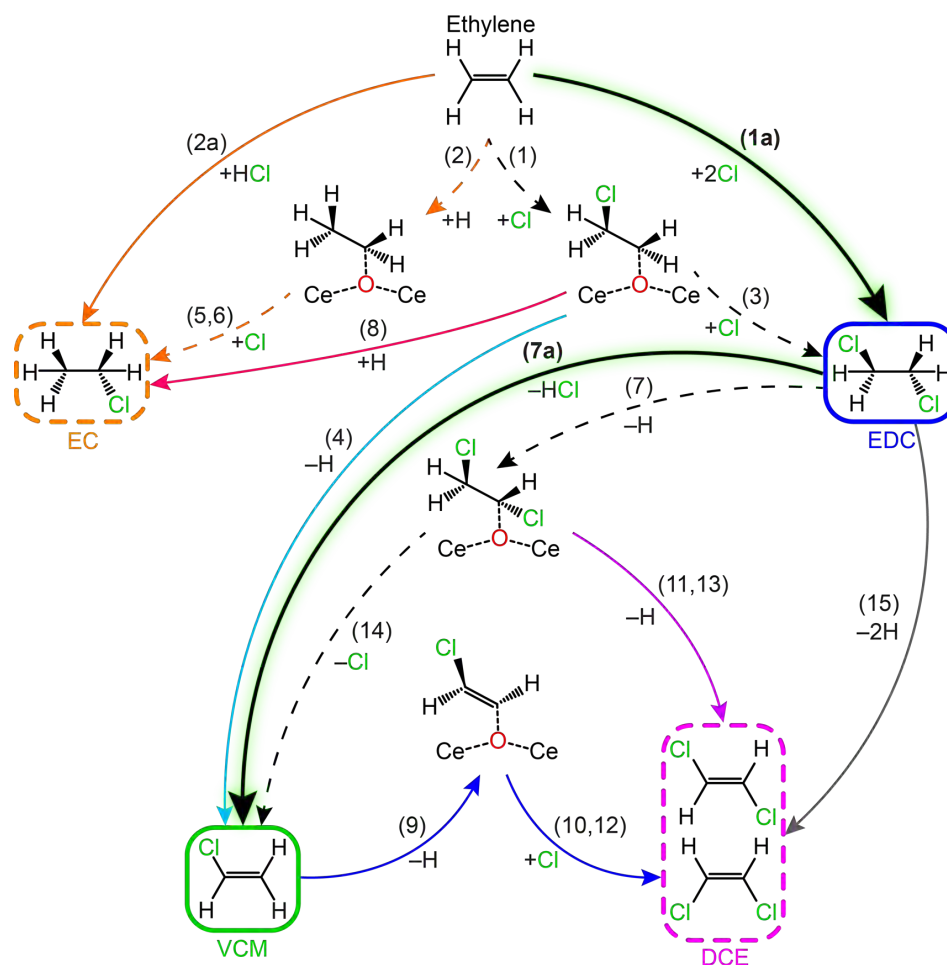
Figure 4. Schematic reaction network showing the main pathway (solid black) leading to EDC and VCM and side pathways either leading VCM (light blue) or leading to chlorinated side-products (orange, magenta, purple, blue, grey). Solid (dashed) boxes indicate desired (undesired) products. For the sake of clarity, all truly reversible reactions are displayed in a single direction. The arrow labels indicate the transferred atom and the reaction number corresponding to Table S2 and Figures S5-12. The main path leading to the desired product is highlighted by the black thick arrows. Dashed arrows represent pathways that were found highly unlikely. Surface-bound intermediates are depicted with a surface excerpt of two Ce and one O atom. Barrier of surface Cl diffusion (step 5): 0.40 eV.

with two chlorinated vacancies ($E_a > 3$ eV). Therefore, it cannot be considered a single elementary step, most likely because it encompasses the rotation that creates the reacting intermediate. On the other hand, the third transition state at reaction coordinate 7 (right inset in Figure 5) involves a truly simultaneous stripping of one chlorine by a vacancy and one hydrogen
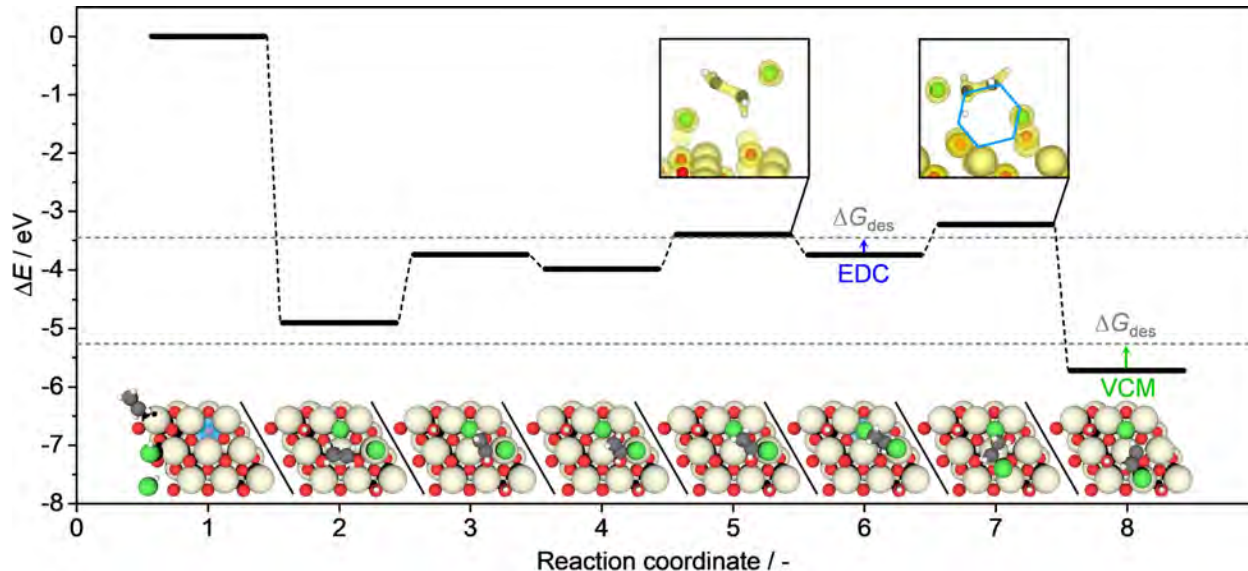
Figure 5. Reaction profile and corresponding optimized structures for ethylene oxychlorination and EDC dehydrochlorination on a defective $CeO_2(111)$ surface (solid black pathway, *i.e.* steps 1a and 7a in Figure 4 and Table S2) including the Gibbs free energy difference for desorption. The reaction coordinates are described in Table 1. The blue glow in the structures highlights a vacancy. The insets depict one individual (left) and a concerted (right) transition state. The yellow overlay represents the charge density (isosurface level 0.2309 Å^{-3}). Color code: oxygen red, cerium yellow, carbon black, chlorine green, hydrogen white.

Table 1. Intermediate, state description, energy with respect to gas phase reactants, ΔE, reaction energy with respect to the previous intermediate, E_r, activation energies, E_a, and imaginary frequencies of transition states, v_i, corresponding to Figure 5. The symbol ■ denotes a lattice oxygen, □ an oxygen vacancy, and * a lattice cerium, respectively. Multiple symbols indicate occupation of multiple sites by the adsorbate. In transition states, the added or stripped atom is indicated with a double dash (--).

Intermediate	State description	ΔE (eV)	E_r (eV)	E_a (eV)	v_i (cm^{-1})
1	$C_2H_4(g)$ + 2 HCl(g) + □ + 2 *+ 2 ■	0	-	-	-
2	C_2H_4* + Cl□ +Cl* +2 H■	−4.90	−4.90	-	-
3	C_2H_4*--Cl□ +Cl* +2 H■	−3.74	-	1.16	254
4	C_2H_4Cl*□ +Cl* +2 H■	−3.99	0.91	-	-
5	C_2H_4Cl*□--Cl* +2 H■	−3.39	-	0.60	239
6	$C_2H_4Cl_2$*□* +2 H■	−3.70	0.29	-	-
7	C_2H_3Cl**--Cl□--H■ +2 H■	−3.22	-	0.48	612
8	C_2H_3Cl** + Cl□ +3 H■	−5.72	−1.94	-	-

by a lattice oxygen, resulting in a barrier of only 0.48 eV. In contrast to the previous steps, this

H-Cl extrusion does not involve a rotation, allowing the creation of a largely stabilized

six-membered ring, formed by the surface and the transition state structure. Plots of the charge density (insets in Figure 5) evidence this hypothesis. Yet, EDC is the dominating product compared to VCM as experimentally observed, which can be explained by the lower ΔG for EDC desorption than the barrier for its transformation to VCM.

In mechanistic investigations through Density Functional Theory, selectivity is retrieved by the comparison of the desired path against potential side routes leading to the same or secondary products. Such an alternative route to form VCM could be offered by dehydrogenation of C_2H_5Cl (EC) or its corresponding intermediate C_2H_4Cl. However, while the latter is in principle possible with a barrier of 1.68 eV (path 4 in Figure 4, Figure 6, Table 2), EC formation itself is highly unlikely. While the stoichiometric surface prohibits EC formation completely, the defect surface allows at least a very easy transformation of a surface alcohol (C_2H_4ClOH) to EC ($E_a = 0.04$ eV). However, such a surface alcohol formation is strongly endothermic ($E_r = 1.5$ eV) and thus the formation of EC can be excluded (path 2, 2a, 5, 6, 8 in Figure 4, Figure S13, Table S3-4).

Formation of the undesired by-products *cis*- and *trans*-DCE is possible through steps 11 and 13 from the surface-bound intermediate $C_2H_3Cl_2$ (Figure S14, Table S5), favoring the *cis* isomer, which reflects the experimental observation. However, this mechanism is rather unlikely as it only works on a stoichiometric surface or patches where no vacancy is near. Otherwise, the concerted step 7a would directly lead to VCM and the necessary surface intermediate would not exist. Furthermore, even on a stoichiometric surface, step 7a exhibits only a barrier of 0.61 eV which is 0.56 eV lower than the formation of the necessary intermediate (step 7), making this path even more unlikely. Both alternative pathways to yield DCE (blue and grey in Figure 4, step 9, 10, 12, 15) with VCM or EDC as a starting point exhibit relatively high barriers. However,

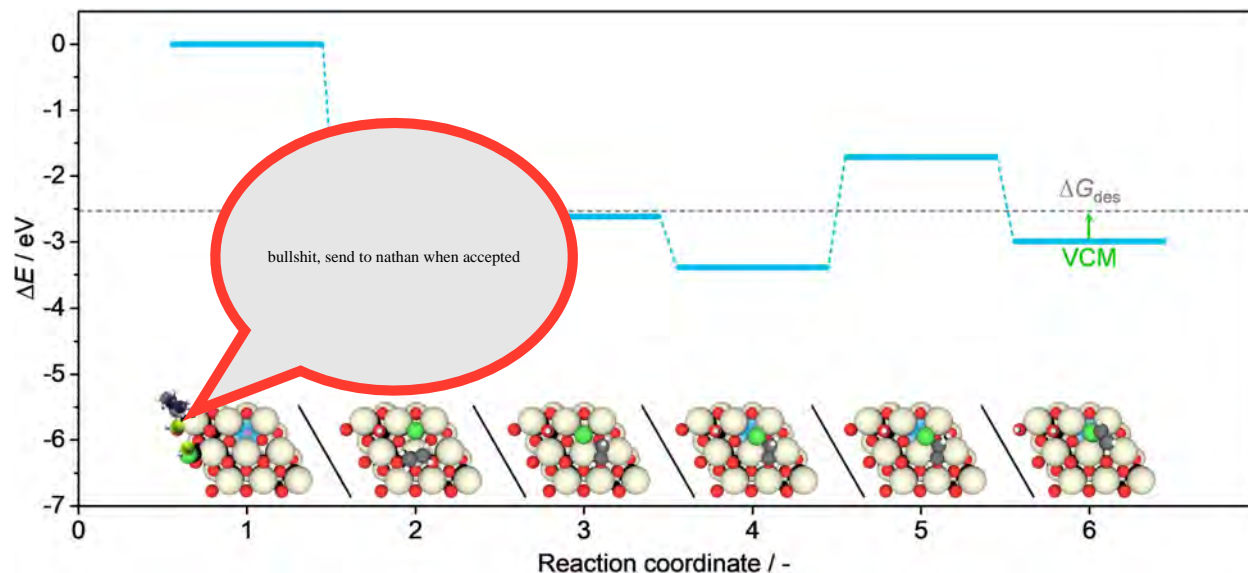**Figure 6.** Reaction profile and corresponding optimized structures for direct VCM formation from ethylene on a defective $CeO_2(111)$ surface (light blue pathway, *i.e.* steps 1 and 4 in Figure 4 and Table S2) including the Gibbs free energy difference for desorption. The reaction coordinates are described in Table 2. The blue glow in the structures highlights a vacancy. Same color code as in Figure 5.

Table 2. Intermediate, state description, energy with respect to gas phase reactants, ΔE, reaction energy with respect to the previous intermediate, E_r, activation energies, E_a, and imaginary frequencies of transition states, ν_i, corresponding to Figure 6. The symbol ■ denotes a lattice oxygen, □ an oxygen vacancy, and * a lattice cerium. Multiple symbols indicate occupation of multiple sites by the adsorbate. In transition states, the added or stripped atom is indicated with a double dash, --.

Intermediate	State description	ΔE (eV)	E_r (eV)	E_a (eV)	ν_i (cm^{-1})
1	$C_2H_4(g) + HCl(g) + □ + * + 2 ■$	0	-	-	-
2	$C_2H_4* + Cl□ + H■ + ■$	−3.79	−3.79	-	-
3	$C_2H_4*--Cl□ + H■ + ■$	−2.61	-	1.18	278
4	$C_2H_4Cl*□ + H■ + ■$	−3.38	−0.40	-	-
5	$C_2H_3Cl*□--H■ + H■$	−1.71	-	1.67	450
6	$C_2H_3Cl*□ + 2 H■$	−2.99	−0.39	-	-

due to strong VCM and even stronger EDC adsorption on a vacancy, the blue and grey paths, both favoring the *cis* isomer, seem to represent the more likely mechanism of DCE formation (Figure 7, Table 3-4). Counterbalancing this process is only the fact that even though VCM or EDC is strongly adsorbed on a vacancy, it can easily be displaced by HCl or O_2 adsorption.
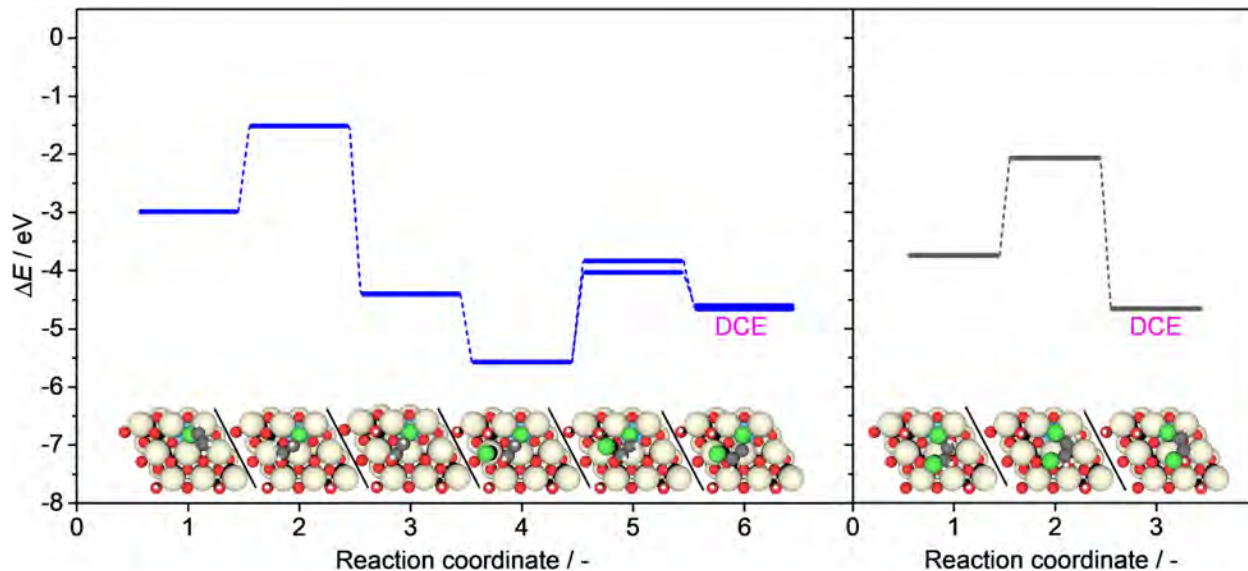
Figure 7. Reaction profile and corresponding optimized structures for DCE formation from VCM (end of step 4, Figure 6) on a defective CeO$_2$ (111) surface through steps 9, 10, and 12 in Figure 4 and Table S2 (left), with the reaction coordinates described in Table 3. Reaction profile and corresponding optimized structures for DCE formation from EDC (end of step 1a-2, Figure 5) on a defective CeO$_2$ (111) surface through step 15 (right), with the reaction coordinates described in Table 4. Same color code as Figure 5.

Table 3. Intermediate, state description, energy with respect to gas phase reactants ΔE, reaction energy with respect to the previous intermediate, E_r, activation energies, E_a, and imaginary frequencies of transition states, v_i, corresponding to Figure 7. The symbol ■ denotes a lattice oxygen, □ an oxygen vacancy, and * a lattice cerium. Multiple symbols indicate occupation of multiple sites by the adsorbate. In transition states, the added or stripped atom is indicated with a double dash, --.

Intermediate	State description	ΔE (eV)	E_r (eV)	E_a (eV)	v_i (cm^{-1})
1	C$_2$H$_3$Cl*□ + 2 H■ + ■	−2.99	-	-	-
2	C$_2$H$_2$Cl*□--H■ + 2 H■	−1.51	-	1.48	1499
3	C$_2$H$_2$Cl*□ + 3 H■ + *+ ■ + HCl(g)	−4.40	−1.41	-	-
4	C$_2$H$_2$Cl*□ + 4 H■ + Cl*	−5.57/−5.94	−1.17/−1.54	-	-
5	c/t-C$_2$H$_2$Cl*□--Cl* + 4 H■	−3.84/−4.04	-	1.73/1.90	376/365
6	c/t-C$_2$H$_2$Cl$_2$*□* + 4 H■	−4.65/−4.59	0.92/1.35	-	-

Oxidation processes were studied by investigating the energy barriers of chemisorption of ethylene and VCM on a molecular O$_2$ in a vacancy, which both rendered very low (0.88 and 1.01 eV). However, the probability of such a setting existing is extremely low, as O$_2$ would easily split up when another vacancy is present (barrier of 0.80 eV), refilling of two vacancies

Table 4. Intermediate, state description, energy with respect to gas phase reactants, ΔE, reaction energy with respect to the previous intermediate, E_r, activation energies, E_a, and imaginary frequencies of transition states, ν_i, corresponding to Figure 7. The symbol ■ denotes a lattice oxygen, □ an oxygen vacancy, and * a lattice cerium. Multiple symbols indicate occupation of multiple sites by the adsorbate. In transition states, the added or stripped atom is indicated with a double dash, --.

Intermediate	State description	ΔE (eV)	E_r (eV)	E_a (eV)	ν_i (cm^{-1})
1	C$_2$H$_4$Cl$_2$*□* +2 H■ + 2■	−3.75	-	-	-
2	C$_2$H$_2$Cl$_2$*□*--H■--H■ +2 H■	−2.12	-	1.63	601
3	c-C$_2$H$_2$Cl$_2$*□* +4 H■	−4.65	−0.90	-	-

(surface and subsurface) is possible,[32] and chemisorption of a (chlorinated) gas phase hydrocarbon is not possible on a lattice oxygen on the CeO$_2$(111) surface. Furthermore, the adsorption energy of HCl is 0.89 eV higher than the one of O$_2$, resulting in the preferential adsorption of HCl. As O$_2$ activation, leaving active O atoms on the surface is unlikely, the lateral oxidation processes have not been investigated further.

3.3. Direct chlorination and gas phase contributions. From previous studies, we know that CeO$_2$ exhibits considerable HCl oxidation activity at conditions close to our reaction conditions,[28,32] prompting an investigation of gas phase and direct chlorination contributions. As depicted in Figure 8a-b, direct chlorination, *i.e.*, addition of Cl$_2$ to ethylene, or formation of VCM through replacement of H by Cl, reaches about 50% conversion over quartz particles and about 60% conversion over CeO$_2$-873 at 673 K. In both cases, VCM is the dominant product. In order to ensure that quartz particles are inert and do not catalyze the reaction, a pure gas phase test was conducted in an empty reactor, yielding the exact same performance (Figure S15a). Considering that under equivalent conditions, Cl$_2$ is formed with 10% conversion over CeO$_2$-873 in HCl oxidation – even CeO$_2$-NC reach 5% conversion (Figure 8c, S15b) – and comparing the oxychlorination activity (Figure 8d) it can be expected that at 673 K about 6-8% in total, might stem from gas phase direct chlorination. Figure 8e depicts the gas phase activation energies of
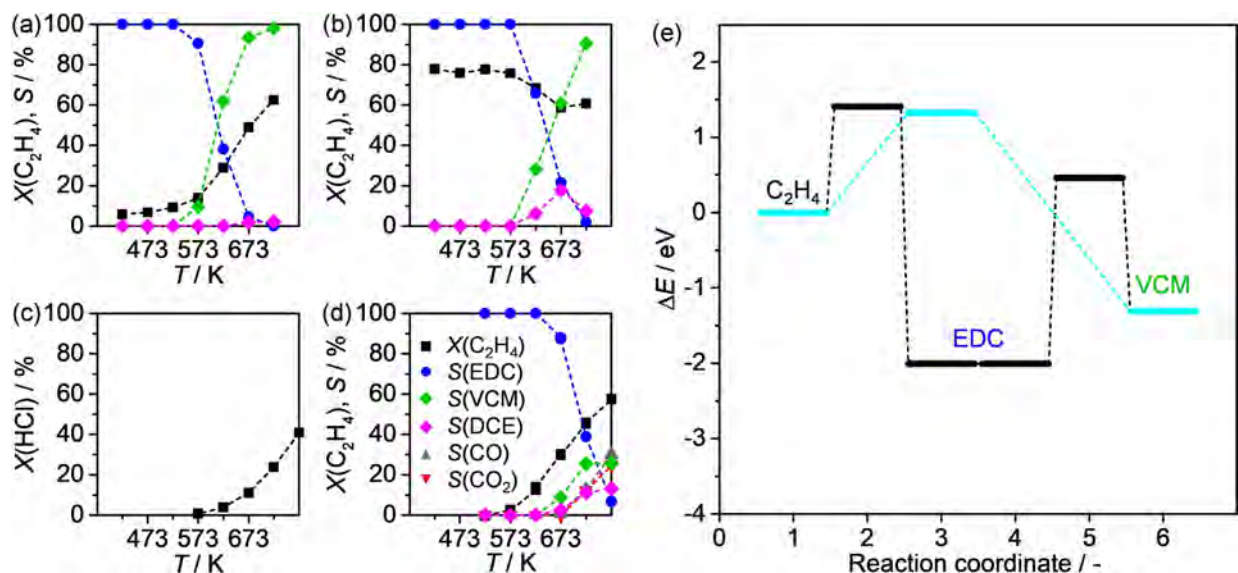
Figure 8. Conversion (*X*) and selectivity (*S*) *versus* temperature in steady state catalytic tests of (a) direct chlorination with C_2H_4:Cl_2 = 3:2.4 on quartz and (b) CeO_2-873, (c) HCl oxidation with HCl:O_2 = 4.8:3 on CeO_2-873, and (d) oxychlorination on CeO_2-873 with C_2H_4:HCl:O_2 = 3:4.8:3. Other conditions: W_{cat} = 0.5 g, F_{tot} = 100 cm³ STP min⁻¹, P = 1 bar. (e) Reaction profile for gas phase ethylene chlorination and subsequent EDC dehydrochlorination (black), and gas phase direct VCM formation from ethylene (light blue).

EDC and VCM formation from ethylene in which direct addition of Cl_2 to ethylene to form EDC yields an energy barrier of 1.41 eV while being exothermic by −2.01 eV. In comparison to this direct addition, the literature also reports the possibility of radical assisted mechanisms for direct halogenation, *e.g.*, hydroxyl assisted direct iodination of aromatics, highlighting the rich chemistry offered by halogenation reactions.[72] The former barrier is only beaten by its lower counterpart (1.32 eV) of direct VCM formation through a one-step dehydrogenation-Cl-addition, where one hydrogen is stripped from ethylene by one Cl while the other Cl transfers to the C_2H_3 radical. The exothermicity of this reaction (−1.31 eV) is however lower than for EDC formation, implying that EDC dehydrochlorination is endothermic by 0.70 eV. In addition, the latter presents a very high energy barrier of 2.47 eV, excluding the dehydrogenation pathway in the gas phase. Even EDC, HCl, or O_2 assisted dehydrochlorination, *i.e.*, presence of one of the above

molecules in the close surroundings of EDC, did not significantly change the barrier. Prompted by this result, we conducted gas phase dehydrochlorination of EDC with and without co-fed HCl or O_2, supporting the calculations as no conversion could be observed until 723 K (6% only for co-fed HCl, no conversion otherwise, Figure S15c). Thus, reactions in the gas phase predominantly yield VCM, as direct VCM formation is favored over EDC formation, while EDC dehydrochlorination is non-existent.

3.4 Temporal analysis of products. In an attempt to corroborate the above described theoretical reaction scheme, we conducted transient experiments with sub-millisecond time resolution on pre-equilibrated CeO_2-873-E673. Figure 9a depicts the height-normalized transient responses of Cl_2, EDC, VCM, and CO_2, recorded after simultaneous pulsing of HCl, C_2H_4, and O_2. Herein, Cl_2 was the first product detected at the reactor outlet followed by EDC, VCM, and finally CO_2. The same product formation sequence was observed in the absence of gas-phase O_2, *i.e.* when only HCl and C_2H_4 were simultaneously pulsed (Figure S16). Notably, neither radicals, nor EC were observed in these experiments, in agreement with the results of steady-state experiments and DFT. Therefore, the pink (8) and orange pathways (2 and 5, 6) of EC formation and its dehydrogenation to VCM in Figure 4 do not contribute to the overall reactivity. However, this does not necessarily exclude the second step of dehydrogenation (path 4 in Figure 4), which could still be part of the direct VCM formation from ethylene, even though not favored. Insight on this circumstance was indirectly derived from analyzing the order of appearance of EDC and VCM (Figure 9a), which suggests that C_2H_4 is initially converted into EDC followed by dehydrochlorination of the latter to VCM. This experimental finding supports the pathways predicted by DFT (*i.e.* $C_2H_4 \rightarrow EDC \rightarrow VCM$, black arrows in Figure 4). As the same sequence of product formation was also observed in the absence of gas-phase O_2 (Figure S16), the above

26

statement should be valid for a broad range of coverage by oxygen and chlorine species, thus supporting the validity of our chosen defect model surface. In addition, this experiment also revealed a correlation between the amount of formed chlorine-containing products (EDC and VCM) and the amount of detected Cl_2 (Figure S17), suggesting that high chlorine coverage favors both the formation of EDC/VCM and desorption of Cl_2. This statement is in line with the hypothesis that both processes take place in parallel and increased temperature, and thus less poisoning through faster Cl_2 evolution, leads to an increased yield of EDC and VCM.

In order to check if the source of chlorine, *i.e.* HCl or Cl_2, influences the pathways of EDC and VCM formation, we performed experiments with simultaneous pulsing of Cl_2, C_2H_4, and O_2. Figure 9b depicts the obtained height-normalized transient responses of EDC, VCM, and CO_2. The order of appearance of these products indicates that EDC is the first chlorinated hydrocarbon formed from ethylene, which is in agreement with tests using HCl as chlorine source. Therefore, the order of the reaction steps including chlorination of C_2H_4 to EDC and subsequent dehydrochlorination of this product to VCM does not depend on the source of chlorine. This
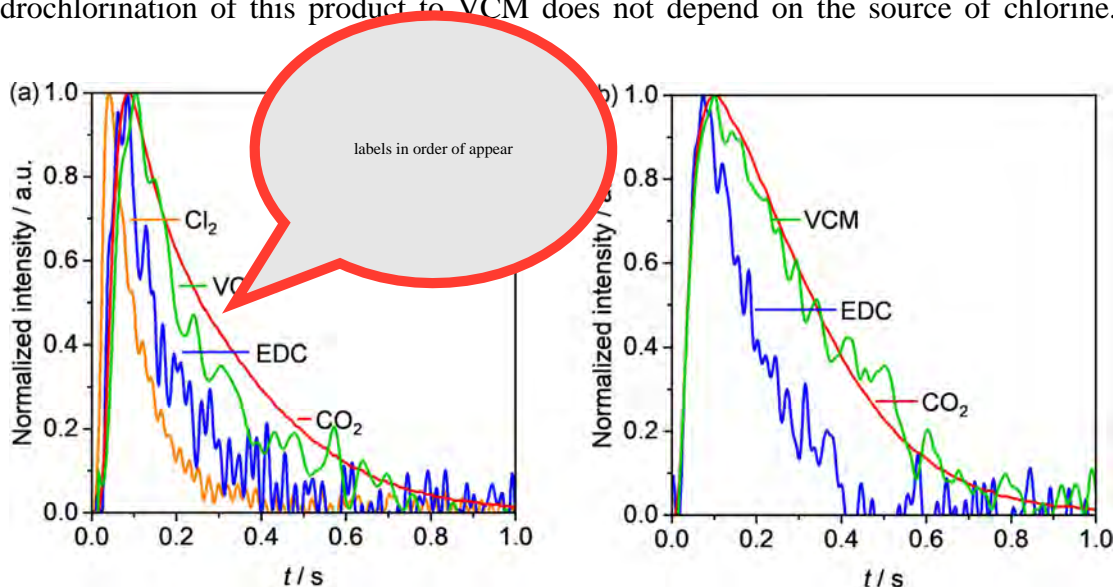
Figure 9. Normalized transient responses of (a) Cl_2, VCM, EDC, and CO_2 upon simultaneous pulsing of HCl:Ar = 1:1 and C_2H_4:O_2:Ne = 1:1:1 at 773 K and (b) VCM, EDC, and CO_2 upon simultaneous pulsing of Cl_2:Ar = 1:1 and C_2H_4:O_2:Ne = 1:1:1 at 773 K.
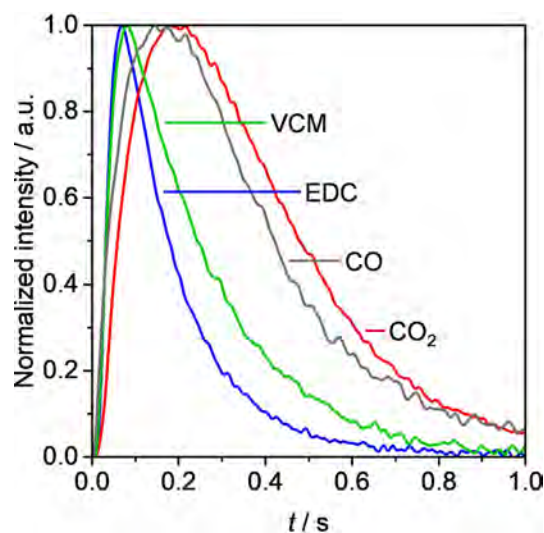
Figure 10. Normalized transient responses of VCM, EDC, CO, and CO_2 upon pulsing of EDC:Ar = 1:6 at 773 K.

statement is in line with the observation in our calculations that both HCl and Cl_2 immediately dissociate upon adsorption, regardless of vacancies being present or not.

In addition, the catalytic ability to dehydrochlorinate EDC was tested in separate experiments, resulting in the transient responses of EDC, VCM, CO, and CO_2 as shown in Figure 10. The first observed product was VCM, further supporting the conclusion about an intermediate role of EDC upon conversion of HCl and C_2H_4 to VCM.

Even though combustion products (CO and CO_2) account for the smallest fraction of products, they are yet substantial and understanding of their formation is important for improving the catalyst performance. CO was not detected when C_2H_4 and O_2 were simultaneously pulsed with HCl or Cl_2 (Figure 9). This is also valid for ethylene oxidation reaction in the absence of Cl-contacting reactants (Figure S18). Although it cannot be completely excluded that CO was formed in tiny amounts, which are below the detection limit, the main unselective pathway of C_2H_4 conversion is its oxidation to CO_2. CO and CO_2 were observed when EDC reacted with the catalyst in the absence of gas-phase O_2. It is also possible that these carbon oxides originated

28

from VCM. Thus, both ethylene and its chlorinated products are responsible for the formation of CO_x in the course of ethylene oxychlorination. In addition, lattice oxygen species appear to actively participate in these undesired processes.

4. CONCLUSIONS

The combination of computational analysis by application of the density functional theory with steady state experiments and investigation of transient kinetics by temporal analysis of products revealed the mechanism of ethylene oxychlorination on CeO_2. Experimental results suggest that the catalytic material consists of an oxide, supporting a surface oxychloride during reaction conditions. In addition, surface alterations by formation and chlorination of vacancies are an important factor determining the selectivity. While empty vacancies decrease the selectivity to EDC or VCM, facilitating their further transformation to DCE, chlorinated vacancies enable the formation of EDC in the first place, as evidenced by an increase of selectivity to desired products with higher surface chlorination. Different facets of ceria ((111) and (100)) did not show significant performance differences except for lower activity of the polar (100) surface, which was related to lower overall surface area and higher chlorination (poisoning) of the sample. Thus, the most stable (111) surface of CeO_2 with one vacancy was chosen as a model catalyst. We revealed that the formation of VCM most likely proceeds through dehydrochlorination of EDC which is greatly facilitated on the defect surface, while pure dehydrogenation pathways that require C_2H_5Cl as an intermediate could be excluded. The major finding, enabling easy EDC to VCM transformation and thus making the proposed pathway feasible, is the ability of ceria to perform concerted elementary steps. Most importantly, of the three types of theoretical concerted steps, HCl, H_2, or Cl_2, addition or abstraction, only HCl

abstraction was found dominating and responsible for the excellent dehydrochlorination behavior of ceria, while H_2 abstraction is feasible. The cause for this easy concerted HCl abstraction can be found in the formation of a hexagonal structure that is formed by the electron densities of the involved C, Cl, H, O, and Ce atoms. Furthermore, formation of other polychlorinated by-products such as DCE is possible either form EDC or VCM, with concerted H abstraction or through individual steps from VCM, given that EDC or VCM are adsorbed on a vacancy. In other words, chlorinated vacancies facilitate the formation of EDC and its dehydrochlorination to VCM, staying chlorinated at the end of the process. However, VCM that is formed through an alternative, yet less important, direct path without EDC as intermediate leads to a non-chlorine-filled vacancy, acting as an anchoring site and increasing its adsorption, which then enables DCE formation. Given that the *cis* isomer is the only experimentally observed product, and EDC also occupies a vacancy after its formation, EDC appears to be more likely to transform to DCE than VCM. These observations are supported by transient kinetic studies that evidenced the oxychlorination-dehydrochlorination pathway by revealing that EDC is always formed as first product, regardless of the chlorine source, followed by VCM. In addition, separate EDC dehydrogenation experiments substantiated this path, while the absence of ethyl chloride intermediates excluded pure dehydrogenation processes for VCM formation. Furthermore, we revealed that CO mostly stems from the combustion of chlorinated hydrocarbons, whereas ethylene yields only CO_2. Gas phase chlorination, mostly yielding VCM, was found to be non-negligible, yet not governing, while EDC dehydrogenation is impossible in the gas phase.

The synergies obtained by the extensive combination of computational, steady state, and transient kinetic analysis in this study allow to shed light on a complex reaction network of an

industrially highly relevant reaction on CeO_2, providing a basis for further development and simulation of oxide or oxychloride based catalysts for oxychlorination reactions.

AUTHOR INFORMATION

Corresponding Authors

* Núria López: nlopez@iciq.es, Javier Pérez-Ramírez: jpr@chem.ethz.ch.

ASSOCIATED CONTENT

Supporting Information. Scheme of oxychlorination set-up, additional characterization and catalytic data, optimized geometries of adsorbed species and initial, transition state, and final geometries of elemental steps, additional reaction profiles, additional TAP data (PDF).

ABBREVIATIONS

EDC: Ethylenedichloride, 1,2-Dichlorethane, $C_2H_4Cl_2$.

VCM: Vinyl chloride monomer, Chloroethene, C_2H_3Cl.

DCE: 1,2-Dichloroethene, $C_2H_2Cl_2$.

EC: Ethylchloride, Chloroethane, C_2H_5Cl.

REFERENCES

(1)   Businesswire. Global Polyvinyl Chloride (PVC) Market Worth USD 72.330 Billion by 2021 http://www.businesswire.com/news/home/20161115006496/en/Global-Polyvinyl-Chloride-PVC-Market-Worth-USD (accessed Sep 24, 2017).

(2)   Johnston, P.; Carthey, N.; Hutchings, G. J.; Discovery, development, and commercialization of gold catalysts for acetylene hydrochlorination, *J. Am. Chem. Soc.* **2015**, *137*, 14548–14557.

(3)   Malta, G.; Kondrat, S. A.; Freakley, S. J.; Davies, C. J.; Lu, L.; Dawson, S.; Thetford, A.; Gibson, E. K.; Morgan, D. J.; Jones, W.; Wells, P. P.; Johnston, P.; Catlow, C. R. A.; Kiely, C. J.; Hutchings, G. J.; Identification of single-site gold catalysis in acetylene hydrochlorination, *Science* **2017**, *355*, 1399–1403.

(4)   Oliver-Meseguer, J.; Doménech-Carbó, A.; Boronat, M.; Leyva-Pérez, A.; Corma, A.; Partial reduction and selective transfer of hydrogen chloride on catalytic gold nanoparticles, *Angew. Chem. Int. Ed.* **2017**, *56*, 6435–6439.

(5)   Weissermel, K.; Arpe, H.-J. In *Industrial Organic Chemistry*; *4*, Wiley-VCH: Weinheim, 2008; pp 217–238.

(6)   Naworski, J. S.; Velez, E. S. In *Applied Industrial Catalysis*; *1*, Academic Press: New York, 1983; pp 239–273.

(7)   Pérez-Ramírez, J.; Mondelli, C.; Schmidt, T.; Schlüter, O. F.-K.; Wolf, A.; Mleczko, L.; Dreier, T.; Sustainable chlorine recycling via catalysed HCl oxidation: from fundamentals to implementation, *Energy Environ. Sci.* **2011**, *4*, 4786–4799.

(8)   Malentacchi, M.; Rubini, C. Oxychlorination catalytic composition for controlling exothermic reactions in a fixed bed. EP 1020222 B1, 2004.

(9)   Muddada, N. B.; Fuglerud, T.; Lamberti, C.; Olsbye, U.; Tuning the activity and selectivity of CuCl$_2$/γ-Al$_2$O$_3$ ethene oxychlorination catalyst by selective promotion, *Top. Catal.* **2014**, *57*, 741–756.

(10)   Muddada, N. B.; Olsbye, U.; Caccialupi, L.; Cavani, F.; Leofanti, G.; Gianolio, D.; Bordiga, S.; Lamberti, C.; Influence of additives in defining the active phase of the ethylene oxychlorination catalyst, *Phys. Chem. Chem. Phys.* **2010**, *12*, 5605–5618.

(11)   Henley, J. P.; Jones, M. E.; Hickman, D. A.; Marshall, K. A.; Reed, D. J.; Clarke, W. D.; Olken, M. M.; Walko, L. E. Process for vinyl chloride manufacture from ethane and ethylene with partial HCl recovery from reactor effluent. US 6933417 B1, 2005.

(12)   Van Rooijen, F. E.; Johan, J.; De Bruijn, A. Catalytic oxychlorination. US 0054708 A1, 2009.

(13)   Loos, M.; Goulon, J.; Bertucci, M.; Bachelard, R.; Structural studies using X.A.S. of the active species catalysing the oxychlorination of ethylene – II, *Physica B Condens. Matter* **1989**, *158*, 188–190.

(14)   Lamberti, C.; Prestipino, C.; Bonino, F.; Capello, L.; Bordiga, S.; Spoto, G.; Zecchina, A.; Diaz Moreno, S.; Cremaschi, B.; Garilli, M.; Marsella, A.; Carmello, D.; Vidotto, S.; Leofanti, G.; The chemistry of the oxychlorination catalyst: an *in-situ*, time-resolved XANES study, *Angew. Chem. Int. Ed.* **2002**, *41*, 2341–2344.

(15)   Carmello, D.; Finocchio, E.; Marsella, A.; Cremaschi, B.; Leofanti, G.; Padovan, M.; Busca, G.; An FT-IR and reactor study of the dehydrochlorination activity of CuCl$_2$/γ-Al$_2$O$_3$-based oxychlorination catalysts, *J. Catal.* **2000**, *191*, 354–363.

(16)   Leofanti, G.; Alumina-supported copper chloride 3. Effect of exposure to ethylene, *J. Catal.* **2001**, *202*, 279–295.

(17) Muddada, N. B.; Olsbye, U.; Fuglerud, T.; Vidotto, S.; Marsella, A.; Bordiga, S.; Gianolio, D.; Leofanti, G.; Lamberti, C.; The role of chlorine and additives on the density and strength of Lewis and Brønsted acidic sites of γ-Al$_2$O$_3$ support used in oxychlorination catalysis: A FTIR study, *J. Catal.* **2011**, *284*, 236–246.

(18) Carrubba, R. V.; Spencer, J. L.; Kinetics of the oxychlorination of ethylene, *Ind. Eng. Chem. Process Des. Dev.* **1970**, *9*, 414–419.

(19) Gelperin, E. I.; Bakshi, Y. M.; Zyskin, A. G.; Snagovsky, Y. S.; Avetisov, A. K.; Kinetics and mechanism of ethylene oxychlorination, *Russ. Chem. Ind.* **1996**, *28*, 356–363.

(20) Gianolio, D.; Muddada, N. B.; Olsbye, U.; Lamberti, C.; Doped-CuCl$_2$/Al$_2$O$_3$ catalysts for ethylene oxychlorination: Influence of additives on the nature of active phase and reducibility, *Nucl. Instruments Methods Phys. Res. B* **2012**, *284*, 53–57.

(21) Leofanti, G.; Marsella, A.; Cremaschi, B.; Garilli, M.; Zecchina, A.; Spoto, G.; Bordiga, S.; Fisicaro, P.; Berlier, G.; Prestipino, C.; Casali, G.; Lamberti, C.; Alumina-supported copper chloride 4. Effect of exposure to O$_2$ and HCl, *J. Catal.* **2001**, *295*, 279–295.

(22) Muddada, N. B.; Olsbye, U.; Leofanti, G.; Gianolio, D.; Bonino, F.; Bordiga, S.; Fuglerud, T.; Vidotto, S.; Marsella, A.; Lamberti, C.; Quantification of copper phases, their reducibility and dispersion in doped-CuCl$_2$/Al$_2$O$_3$ catalysts for ethylene oxychlorination, *Dalt. Trans.* **2010**, *39*, 8437–8449.

(23) Magistro, A. J.; Cowfer, J. A.; Oxychlorination of ethylene, *J. Chem. Educ.* **1986**, *63*, 1056–1058.

(24) Wachi, S.; Asai, Y.; Kinetics of 1,2-dichloroethane formation from ethylene and cupric chloride, *Ind. Eng. Chem. Res.* **1994**, *33*, 259–264.

(25) Kurta, S. A.; Investigating active centers of industrial catalysts for the oxidative

chlorination of ethylene on a γ-Al$_2$O$_3$ surface, *Catal. Ind.* **2011**, *3*, 136–143.

(26)   Kurta, S. A.; Catalysis of ethylene oxychlorination into 1,2-dichlorethane in the presence of CuCl$_2$/CuCl active centers on the surface of γ-Al$_2$O$_3$, *Chem. Chem. Technol.* **2012**, *6*, 1–8.

(27)   Scharfe, M.; Lira-Parada, P. A.; Paunovic, V.; Moser, M.; Amrute, A. P.; Pérez-Ramírez, J.; Oxychlorination-dehydrochlorination chemistry on bifunctional ceria catalysts for intensified vinyl chloride production, *Angew. Chem. Int. Ed.* **2016**, *55*, 3068–3072.

(28)   Scharfe, M.; Lira-Parada, P. A.; Amrute, A. P.; Mitchell, S.; Pérez-Ramírez, J.; Lanthanide compounds as catalysts for the one-step synthesis of vinyl chloride from ethylene, *J. Catal.* **2016**, *344*, 524–534.

(29)   Higham, M. D.; Scharfe, M.; Capdevila-Cortada, M.; Pérez-Ramírez, J.; López, N.; Mechanism of ethylene oxychlorination over ruthenium oxide, *J. Catal.* **2017**, *353*, 171–180.

(30)   Montini, T.; Melchionna, M.; Monai, M.; Fornasiero, P.; Fundamentals and catalytic applications of CeO$_2$-based materials, *Chem. Rev.* **2016**, *116*, 5987–6041.

(31)   Paier, J.; Penschke, C.; Sauer, J.; Oxygen defects and surface chemistry of ceria: quantum chemical studies compared to experiment, *Chem. Rev.* **2013**, *113*, 3949–3985.

(32)   Amrute, A. P.; Mondelli, C.; Moser, M.; Novell-Leruth, G.; López, N.; Rosenthal, D.; Farra, R.; Schuster, M. E.; Teschner, D.; Schmidt, T.; Pérez-Ramírez, J.; Performance, structure, and mechanism of CeO$_2$ in HCl oxidation to Cl$_2$, *J. Catal.* **2012**, *286*, 287–297.

(33)   Capdevila-Cortada, M.; Łodziana, Z.; López, N.; Performance of DFT+U approaches in the study of catalytic materials, *ACS Catal.* **2016**, *6*, 8370–8379.

(34)   Loschen, C.; Carrasco, J.; Neyman, K. M.; Illas, F.; First-principles LDA+U and GGA+U

study of cerium oxides: Dependence on the effective U parameter, *Phys. Rev. B* **2007**, *75*, 35115.

(35) Vilé, G.; Albani, D.; Almora-Barrios, N.; López, N.; Pérez-Ramírez, J.; Advances in the design of nanostructured catalysts for selective hydrogenation, *ChemCatChem* **2016**, *8*, 21–33.

(36) Carrasco, J.; Vilé, G.; Fernández-Torre, D.; Pérez, R.; Pérez-Ramírez, J.; Ganduglia-Pirovano, M. V.; Molecular-level understanding of CeO_2 as a catalyst for partial alkyne hydrogenation, *J. Phys. Chem. C* **2014**, *118*, 5352–5360.

(37) Farra, R.; Eichelbaum, M.; Schlögl, R.; Szentmiklósi, L.; Schmidt, T.; Amrute, A. P.; Mondelli, C.; Pérez-Ramírez, J.; Teschner, D.; Do observations on surface coverage-reactivity correlations always describe the true catalytic process? A case study on ceria, *J. Catal.* **2013**, *297*, 119–127.

(38) López, N.; Gómez-Segura, J.; Marín, R. P.; Pérez-Ramírez, J.; Mechanism of HCl oxidation (Deacon process) over RuO_2, *J. Catal.* **2008**, *255*, 29–39.

(39) Over, H.; Atomic-scale understanding of the HCl oxidation over RuO_2, a novel deacon process, *J. Phys. Chem. C* **2012**, *116*, 6779–6792.

(40) Moser, M.; Paunovic, V.; Guo, Z.; Szentmiklósi, L.; Hevia, M. G.; Higham, M.; López, N.; Teschner, D.; Pérez-Ramírez, J.; Interplay between surface chemistry and performance of rutile-type catalysts for halogen production, *Chem. Sci.* **2016**, *7*, 2996–3005.

(41) Farra, R.; Girgsdies, F.; Frandsen, W.; Hashagen, M.; Schlögl, R.; Teschner, D.; Synthesis and catalytic performance of CeOCl in Deacon reaction, *Catal. Lett.* **2013**, *143*, 1012–1017.

(42) Wu, Q.; Zhang, F.; Xiao, P.; Tao, H.; Wang, X.; Hu, Z.; Lü, Y.; Great influence of anions

for controllable synthesis of CeO$_2$ nanostructures: from nanorods to nanocubes, *J. Phys. Chem. C* **2008**, *112*, 17076–17080.

(43)   Wu, Z.; Li, M.; Howe, J.; Meyer, H. M.; Overbury, S. H.; Probing defect sites on CeO$_2$ nanocrystals with well-defined surface planes by Raman spectroscopy and O$_2$ adsorption, *Langmuir* **2010**, *26*, 16595–16606.

(44)   Aneggi, E.; Wiater, D.; de Leitenburg, C.; Llorca, J.; Trovarelli, A.; Shape-dependent activity of ceria in soot combustion, *ACS Catal.* **2014**, *4*, 172–181.

(45)   Brunauer, Stephen; Emmet, P. H.; Teller, E.; Adsorption of gases in multimolecular layers, *J. Am. Chem. Soc.* **1938**, *60*, 309–319.

(46)   Pérez-Ramírez, J.; Kondratenko, E. V.; Evolution, achievements, and perspectives of the TAP technique, *Catal. Today* **2007**, *121*, 160–169.

(47)   Gleaves, J. T.; Yablonsky, G.; Zheng, X.; Fushimi, R.; Mills, P. L.; Temporal analysis of products (TAP) – Recent advances in technology for kinetic analysis of multi-component catalysts, *J. Mol. Catal. A Chem.* **2010**, *315*, 108–134.

(48)   Morgan, K.; Maguire, N.; Fushimi, R.; Gleaves, J. T.; Goguet, A.; Harold, M. P.; Kondratenko, E. V; Menon, U.; Schuurman, Y.; Yablonsky, G. S.; Forty years of temporal analysis of products, *Catal. Sci. Technol.* **2017**, *7*, 2416–2439.

(49)   Kresse, G.; Hafner, J.; Ab initio molecular dynamics for liquid metals, *Phys. Rev. B* **1993**, *47*, 558–561.

(50)   Kresse, G.; Furthmüller, J.; Efficient iterative schemes for ab initio total-energy calculations using a plane-wave basis set, *Phys. Rev. B* **1996**, *54*, 11169–11186.

(51)   Kresse, G.; Furthmüller, J.; Efficiency of ab-initio total energy calculations for metals and semiconductors using a plane-wave basis set, *Comput. Mater. Sci.* **1996**, *6*, 15–50.

(52) Perdew, J. P.; Burke, K.; Ernzerhof, M.; Generalized gradient approximation made simple, *Phys. Rev. Lett.* **1996**, *77*, 3865–3868.

(53) Blöchl, P. E.; Projector augmented-wave method, *Phys. Rev. B* **1994**, *50*, 17953–17979.

(54) Hubbard, J.; Electron correlations in narrow energy bands, *Proc. R. Soc. Lond. A. Math. Phys. Sci.* **1963**, *276*, 238–257.

(55) Grimme, S.; Anthony, J.; Ehrlich, S.; Krieg, H.; A consistent and accurate ab initio parametrization of density functional dispersion correction (DFT-D) for the 94 elements H-Pu, *J. Chem. Phys.* **2010**, *132*, 154104–154122.

(56) Kümmerle, E. A.; Heger, G.; The structures of C–$Ce_2O_{3+\delta}$, Ce_7O_{12}, and $Ce_{11}O_{20}$, *J. Solid State Chem.* **1999**, *147*, 485–500.

(57) Capdevila-Cortada, M.; López, N.; Entropic contributions enhance polarity compensation for CeO_2(100) surfaces, *Nat Mater* **2017**, *16*, 328–334.

(58) Henkelman, G.; Uberuaga, B. P.; Jónsson, H.; A climbing image nudged elastic band method for finding saddle points and minimum energy paths, *J. Chem. Phys.* **2000**, *113*, 9901–9904.

(59) Henkelman, G.; Jónsson, H.; Improved tangent estimate in the nudged elastic band method for finding minimum energy paths and saddle points, *J. Chem. Phys.* **2000**, *113*, 9978–9985.

(60) Álvarez-Moreno, M.; de Graaf, C.; López, N.; Maseras, F.; Poblet, J. M.; Bo, C.; Managing the computational chemistry big data problem: The ioChem-BD platform, *J. Chem. Inf. Model.* **2015**, *55*, 95–103.

(61) https://doi.org/10.19061/iochem-bd-6-5

(62) Frisch, M. J.; Trucks, G. W.; Schlegel, H. B.; Scuseria, G. E.; Robb, M. A.; Cheeseman, J.

R.; Montgomery, J. A.; Vreven, T.; Kudin, K. N.; Burant, J. C.; Millam, J. M.; Iyengar, S. S.; Tomasi, J.; Barone, V.; Mennucci, B.; Cossi, M.; Scalmani, G.; Rega, N.; Petersson, G. A.; Nakatsuji, H.; Hada, M.; Ehara, M.; Toyota, K.; Fukuda, R.; Hasegawa, J.; Ishida, M.; Nakajima, T.; Honda, Y.; Kitao, O.; Nakai, H.; Klene, M.; Li, X.; Knox, J. E.; Hratchian, H. P.; Cross, J. B.; Adamo, C.; Jaramillo, J.; Gomperts, R.; Stratmann, R. E.; Yazyev, O.; Austin, A. J.; Cammi, R.; Pomelli, C.; Ochterski, J. W.; Ayala, P. Y.; Morokuma, K.; Voth, G. A.; Salvador, P.; Dannenberg, J. J.; Zakrzewski, V. G.; Dapprich, S.; Daniels, A. D.; Strain, M. C.; Farkas, O.; Malick, D. K.; Rabuck, A. D.; Raghavachari, K.; Foresman, J. B.; Ortiz, J. V.; Cui, Q.; Baboul, A. G.; Clifford, S.; Cioslowski, J.; Stefanov, B. B.; Liu, G.; Liashenko, A.; Piskorz, P.; Komaromi, I.; Martin, R. L.; Fox, D. J.; Keith, T.; Al-Laham, M. A.; Peng, C. Y.; Nanayakkara, A.; Challacombe, M.; Gill, P. M. W.; Johnson, B.; Chen, W.; Wong, M. W.; Gonzalez, C.; Pople, J. A. *Gaussian Inc., Pittsburgh PA* **2003**.

(63) Ochterski, J. W.; Thermochemistry in Gaussian, *Gaussian Inc., Pittsburgh PA* **2000**.

(64) Li, C.; Sun, Y.; Djerdj, I.; Voepel, P.; Sack, C.-C.; Weller, T.; Ellinghaus, R.; Sann, J.; Guo, Y.; Smarsly, B. M.; Over, H.; Shape-controlled CeO_2 nanoparticles: stability and activity in the catalyzed HCl oxidation reaction, *ACS Catal.* **2017**, *7*, 6453–6463.

(65) Leyva-Pérez, A.; Cómbita-Merchán, D.; Cabrero-Antonino, J. R.; Al-Resayes, S. I.; Oxyhalogenation of activated arenes with nanocrystalline ceria, *ACS Catal.* **2013**, *3*, 250–258.

(66) Trovarelli, A.; Llorca, J.; Ceria catalysts at nanoscale: how do crystal shapes shape catalysis?, *ACS Catal.* **2017**, *7*, 4716–4735.

(67) Kepiński, L.; Wolcyrz, M.; Okal, J.; Effect of chlorine on microstructure and activity of

Pd/CeO$_2$ catalysts, *J. Chem. Soc. Faraday Trans.* **1995**, *91*, 507–515.

(68) Kepiński, L.; Okal, J.; Occurrence and Mechanism of Formation of CeOCl in Pd/CeO$_2$ Catalysts, *J. Catal.* **2000**, *192*, 48–53.

(69) Fajardie, F.; Tempere, O.; Manoli, J.-M.; Djega-Mariadassou, G.; Blanchard, G.; Ceria lattice oxygen ion substitution by Cl$^-$ during the reduction of Rh(Cl)/CeO$_2$ catalysts. Formation and stability of CeOCl, *J. Chem. Soc. Faraday Trans.* **1998**, *94*, 3727–3735.

(70) De Rivas, B.; López-Fonseca, R.; Gutiérrez-Ortiz, M. A.; Gutiérrez-Ortiz, J. I.; Impact of induced chlorine-poisoning on the catalytic behaviour of Ce$_{0.5}$Zr$_{0.5}$O$_2$ and Ce$_{0.15}$Zr$_{0.85}$O$_2$ in the gas-phase oxidation of chlorinated VOCs, *Appl. Catal. B Environ.* **2011**, *104*, 373–381.

(71) García-Melchor, M.; Bellarosa, L.; López, N.; Unique reaction path in heterogeneous catalysis: the concerted semi-hydrogenation of propyne to propene on CeO$_2$, *ACS Catal.* **2014**, *4*, 4015–4020.

(72) Zhang, P; Sun, D.; Wen, M.; Yang, J.; Zhou, K.; Wang, Z.; Hydroxyl radical promotest he direct iodination of aromatic compounds with iodine in water: A combined experimental and theoretical study, *Adv. Synth. Catal.* **2012**, *354*, 720–729.

TABLE OF CONTENTS GRAPHIC
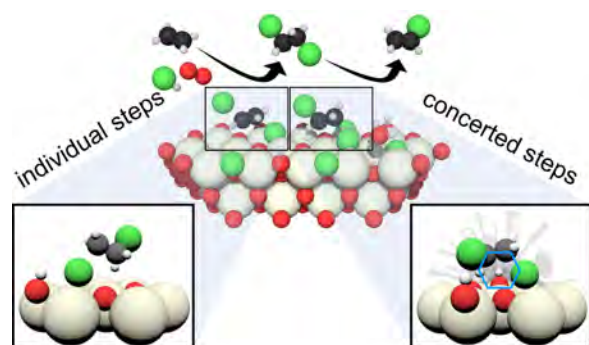
Supporting Information

Mechanism of Ethylene Oxychlorination on Ceria

Matthias Scharfe[†], Marçal Capdevila-Cortada[‡], Vita A. Kondratenko[§], Evgenii V. Kondratenko[§],
Sara Colussi[∥], Alessandro Trovarelli[∥], Núria López[‡,], and Javier Pérez-Ramírez[†,*]*

[†] Institute for Chemical and Bioengineering, Department of Chemistry and Applied Biosciences, ETH Zurich, Vladimir-Prelog-Weg 1, 8093 Zurich, Switzerland.

[‡] Institute of Chemical Research of Catalonia (ICIQ), The Barcelona Institute of Science and Technology, Av. Països Catalans 16, 43007 Tarragona, Spain.

[§] Leibniz-Institut für Katalyse e. V., Albert-Einstein-Straße 29a, 18059 Rostock, Germany.

[∥] Dipartimento Politecnico, Università di Udine, via del Cotonificio 108, 33010 Udine, Italy.

[*] Corresponding authors. Núria López: nlopez@iciq.es, Javier Pérez-Ramírez: jpr@chem.ethz.ch.
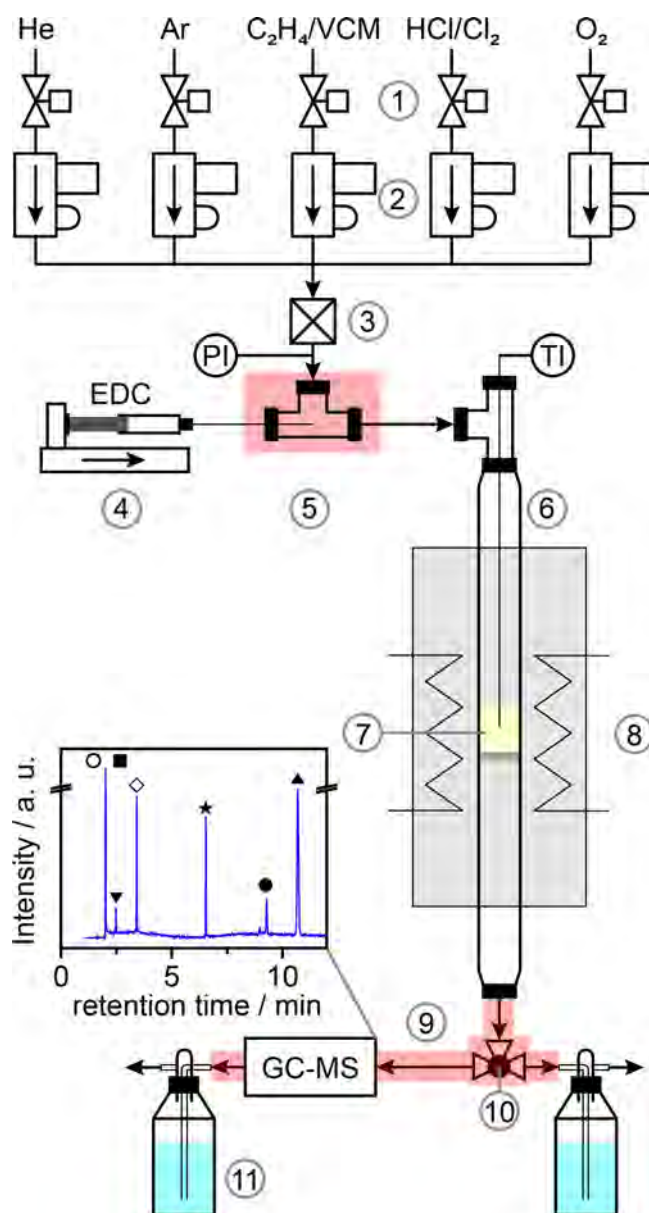
Scheme S1. Scheme of the laboratory set-up used for catalytic studies. 1: on-off valves, 2: mass flow controllers, 3: mixer, 4: syringe pump, 5: vaporizer, 6: quartz reactor, 7: catalyst bed, 8: oven, 9: heat tracing, 10: three-way sampling valve, 11: NaOH scrubbers, PI: pressure indicator, and TI: temperature indicator. The inset depicts a representative chromatogram. The peaks are assigned to the following compounds: ○,■ Ar and CO (subsequently separated by mass spectrometry), ▼ CO_2, ◇ C_2H_4, ★ vinyl chloride, ● 1,2-cis-dichloroethene, and ▲ ethylene dichloride.

Table S1. Total surface area and chlorine content of the ceria samples prior to and after (-E673) ethylene oxychlorination.

Sample	$S_{BET}{}^{a}$ ($m^2\ g^{-1}$)	Cl^{b} (at.%)
CeO$_2$-873	55	0
CeO$_2$-873-E673	39	2.4
CeO$_2$-873-p873-E673	34	2.5
CeO$_2$-NC	19	0
CeO$_2$-NC-E673	17	10.7

[a] BET method.

[b] XRF (Orbis PC Micro-EDXRF).

Table S2. Reaction number, elementary step, step number according to Figure 4, model surface (s for stoichiometric, d for defective), reaction energy, activation energy, and imaginary frequency of the corresponding transition state. The symbol ■ denotes a lattice oxygen, □ an oxygen vacancy, and * a lattice cerium. Multiple symbols indicate occupation of multiple sites by the adsorbate.

#	Elementary step	Step No.	Surface	E_r (eV)	E_a (eV)	v_i (cm^{-1})
1	$C_2H_4(g) + * \rightarrow C_2H_4*$		s	−0.39	-	-
2	$C_2H_4(g) + * \rightarrow C_2H_4*$		d	−0.67	-	-
3	$C_2H_4* + ■ + Cl* \rightarrow C_2H_4Cl■* + *$	1	s	−0.92	1.42	290
4	$C_2H_4* + ■ + Cl□ \rightarrow C_2H_4Cl■□ + *$	1	d	0.41	1.18	278
5	$C_2H_4* + Cl□ + Cl* \rightarrow C_2H_4Cl** + Cl□$	1a-1	d	0.91	1.16	254
6	$C_2H_4Cl** + Cl□ \rightarrow C_2H_4Cl_2**□$	1a-2	d	0.29	0.60	239
7	$C_2H_4Cl■* + Cl* \rightarrow C_2H_4Cl_2■**$	3	s	0.77	1.98	458
8	$C_2H_4Cl■□ + Cl* \rightarrow C_2H_4Cl_2■□*$	3	d	0.69	2.77	500
9	$C_2H_4Cl_2■** \rightarrow C_2H_4Cl_2(g) + ■ + 2 *$		s	0.59	-	-
10	$C_2H_4Cl_2■□* \rightarrow C_2H_4Cl_2(g) + ■ + □ +*$		d	1.23	-	-
11	$C_2H_4Cl_2■** + ■ \rightarrow C_2H_3Cl_2■** + H■$	7	s	−1.62	1.17	581
12	$C_2H_4Cl_2■□* + ■ \rightarrow C_2H_3Cl■* + H■ + Cl□$	7	d	-	-	-
13	$C_2H_3Cl_2■** \rightarrow C_2H_3Cl■* + Cl*$	14	s	-	-	-
14	$C_2H_3Cl_2■□* \rightarrow C_2H_3Cl■* + Cl□$	14	d	-	-	-
15	$C_2H_4Cl_2■** + ■ + * \rightarrow C_2H_3Cl■* + H■ + Cl* +*$	7a	s	−0.78	0.61	935
16	$C_2H_4Cl_2■** + ■ + □ \rightarrow C_2H_3Cl■* + H■ + Cl□ +*$	7a	d	−1.94	0.48	612
17	$C_2H_4Cl■* + ■ \rightarrow C_2H_3Cl■* + H■$	4	s	0.71	1.71	473
18	$C_2H_4Cl■□ + ■ \rightarrow C_2H_3Cl■□ + H■$	4	d	0.39	1.67	450
19	$C_2H_3Cl■* \rightarrow C_2H_3Cl(g) + ■ + *$		s	0.33	-	-
20	$C_2H_3Cl■□ \rightarrow C_2H_3Cl(g) + ■ + □$		d	1.16	-	-
21	$C_2H_4* + ■ + H■ \rightarrow C_2H_5■ + ■ + *$	2	s	−0.30	1.03	583
22	$C_2H_4* + ■ + Cl□ + H■ \rightarrow C_2H_5Cl■□ + ■ + *$	2	d	-	-	-
23	Cl* diffusion	5	s	0.16	0.40	66
24	$C_2H_5■ + Cl* \rightarrow C_2H_5Cl■*$	6	s	0.42	2.10	480
25	$C_2H_5■ + Cl□ \rightarrow C_2H_5Cl■□$	6	d	-	-	-
26	$C_2H_4*+ Cl□ + H■ \rightarrow C_2H_5Cl*□ + ■$	2a	d	1.56	2.08	373
27	$C_2H_4Cl■* + H■ \rightarrow C_2H_5Cl■* + ■$	8	s	-	-	-
28	$C_2H_4Cl□■H \rightarrow C_2H_5Cl■□$	8	d	−0.40	0.04	362
29	$C_2H_5Cl■* \rightarrow C_2H_5Cl(g) + ■ + *$		s	0.51	-	-
30	$C_2H_5Cl■□ \rightarrow C_2H_5Cl(g) + ■ + □$		d	1.24	-	-
31	$C_2H_3Cl■* + ■ \rightarrow C_2H_2Cl■* +H■$	9	s	−2.01	1.44	.
32	$C_2H_3Cl■□ + ■ \rightarrow C_2H_2Cl■□ +H■$	9	d	−1.41	1.48	1499
33	$C_2H_2Cl■* + Cl* \rightarrow c\text{-}C_2H_2Cl_2■**$	10	s	2.27	1.53	501
34	$C_2H_2Cl■□ + Cl* \rightarrow c\text{-}C_2H_2Cl_2■□*$	10	d	1.73	0.92	376
35	$C_2H_2Cl■* + Cl* \rightarrow t\text{-}C_2H_2Cl_2■**$	12	s	1.99	1.28	393
36	$C_2H_2Cl■□ + Cl* \rightarrow t\text{-}C_2H_2Cl_2■□*$	12	d	1.91	1.35	365
37	$C_2H_3Cl_2■* + ■ \rightarrow c\text{-}C_2H_2Cl_2■* + H■$	11	s	1.20	0.83	1034
38	$C_2H_3Cl_2■□ + ■ \rightarrow c\text{-}C_2H_2Cl_2■□ + H■$	11	d	0.96	1.08	1192
39	$C_2H_3Cl_2■* + ■ \rightarrow t\text{-}C_2H_2Cl_2■* + H■$	13	s	1.75	0.75	435
40	$C_2H_3Cl_2■□ + ■ \rightarrow t\text{-}C_2H_2Cl_2■□ + H■$	13	d	1.19	1.10	1073
41	$c\text{-}C_2H_2Cl_2■** \rightarrow c\text{-}C_2H_2Cl_2(g) + ■ + 2 *$		s	0.52	-	-
42	$c\text{-}C_2H_2Cl_2■□* \rightarrow c\text{-}C_2H_2Cl_2(g) + ■ + □ + *$		d	1.18	-	-
43	$t\text{-}C_2H_2Cl_2■** \rightarrow t\text{-}C_2H_2Cl_2(g) + ■ + 2 *$		s	0.50	-	-
44	$t\text{-}C_2H_2Cl_2■□* \rightarrow t\text{-}C_2H_2Cl_2(g) + ■ + □ + *$		d	1.12	-	-
45	$C_2H_4Cl_2■□* + 2 ■ \rightarrow c\text{-}C_2H_2Cl_2■□* + 2 H■$	15	d	−0.90	1.63	601
46	$C_2H_4Cl_2■□* + 2 ■ \rightarrow t\text{-}C_2H_2Cl_2■□* + 2 H■$	15	d	-	-	-

Table S3. Intermediate, state description, energy with respect to gas phase reactants ΔE, reaction energy with respect to the previous intermediate E_r, activation energies E_a, and imaginary frequencies of transition states ν_i, corresponding to **Figure S13a**. The symbol ■ denotes a lattice oxygen, □ an oxygen vacancy, and * a lattice cerium. Multiple symbols indicate occupation of multiple sites by the adsorbate. In transition states, the added or stripped atom is indicated with a double dash --.

Intermediate	State description	ΔE (eV)	E_r (eV)	E_a (eV)	ν_i (cm^{-1})
1	C_2H_4(g) + HCl(g) + □ + *+ ■	0	-	-	-
2	C_2H_4* + Cl□ + H■	−3.79	-3.79	-	-
3	C_2H_4*--Cl□ + H■	−2.61	-	1.18	278
4	C_2H_4Cl*□ + H■	−3.39	-0.40	-	-
5	C_2H_4ClOH*□□	−1.80	1.59	-	-
6	C_2H_4Cl*□--H■	−1.75	-	0.05	362
7	C_2H_5Cl*□ + ■	−2.19	−0.44	-	-

Table S4. Intermediate, state description, energy with respect to gas phase reactants ΔE, reaction energy with respect to the previous intermediate E_r, activation energies E_a, and imaginary frequencies of transition states ν_i, corresponding to **Figure S13b**. The symbol ■ denotes a lattice oxygen, □ an oxygen vacancy, and * a lattice cerium. Multiple symbols indicate occupation of multiple sites by the adsorbate. In transition states, the added or stripped atom is indicated with a double dash --.

Intermediate	State description	ΔE (eV)	E_r (eV)	E_a (eV)	ν_i (cm^{-1})
1	C_2H_4(g) + HCl(g) + □ + *+ ■	0	-	-	-
2	C_2H_4* + Cl□ + H■	−3.79	3.79	-	-
3	C_2H_4*--Cl□--H■	−1.68	-	2.11	373
4	C_2H_5Cl*□ + ■	−2.20	1.59	-	-

Table S5. Intermediate, state description, energy with respect to gas phase reactants ΔE, reaction energy with respect to the previous intermediate E_r, activation energies E_a, and imaginary frequencies of transition states v_i, corresponding to **Figure S14**. The symbol ■ denotes a lattice oxygen, □ an oxygen vacancy, and * a lattice cerium. Multiple symbols indicate occupation of multiple sites by the adsorbate. In transition states, the added or stripped atom is indicated with a double dash --.

Intermediate	State description	ΔE (eV)	E_r (eV)	E_a (eV)	v_i (cm^{-1})
1	C_2H_4(g) + HCl(g) + 2 *+ ■	0	-	-	-
2	C_2H_4* + Cl* + H■	−1.90	1.90	-	-
3	C_2H_4*--Cl* + H■	−0.48	-	1.42	290
4	C_2H_4Cl** + H■ + HCl(g) + * + ■	−2.82	-	-	-
5	C_2H_4Cl** + 2 H■ + Cl*	−4.33	−1.51	-	-
6	C_2H_4Cl**--Cl* + 2 H■ + 2 ■	−2.35	-	1.98	458
7	$C_2H_4Cl_2$*** + 2 H■+ ■	−3.55	0.78	-	-
8	$C_2H_3Cl_2$***--H■ + 2 H■	−2.14	-	1.41	581
9	$C_2H_3Cl_2$*** + 3 H■ + ■	−4.94	−1.39	-	-
10	c/t-$C_2H_2Cl_2$***--H■ + 3 H■	−3.78/−3.22	-	1.16/1.72	1034/435
11	c/t-$C_2H_2Cl_2$*** + 4 H■	−4.15/−4.23	−2.01/−2.09		-
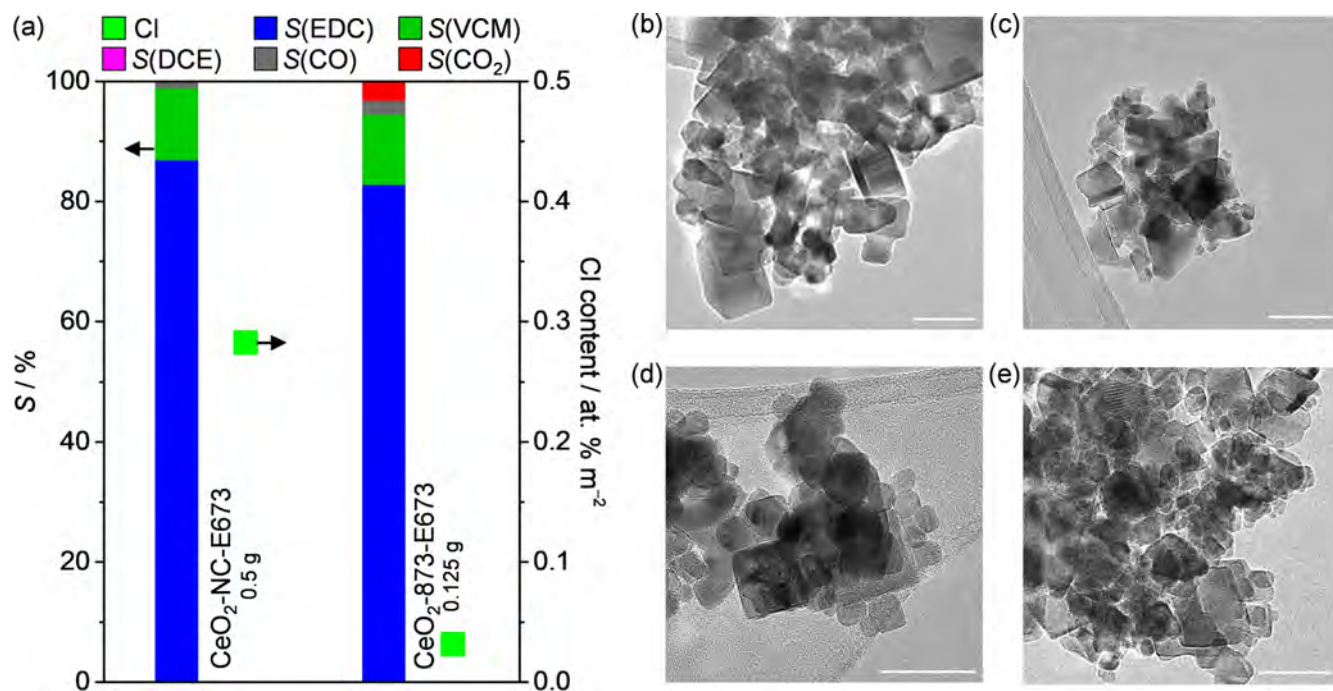
Figure S1. (a) Selectivity (bars) and chlorine content (squares) of CeO$_2$–NC-E673 and CeO$_2$-873-E673 compared at the same degree of ethylene conversion (16%). Conditions: T = 673 K, C$_2$H$_4$:HCl:O$_2$ = 3:4.8:3, P = 1 bar, F_{tot} = 100 cm^3 STP min^{-1}, time-on-stream 2 h. HRTEM images of (b) CeO$_2$-NC, (c) CeO$_2$-873, (d) CeO$_2$-NC-E673, and (e) CeO$_2$-873-E673. The scale bars in the micrographs represent 50 nm.
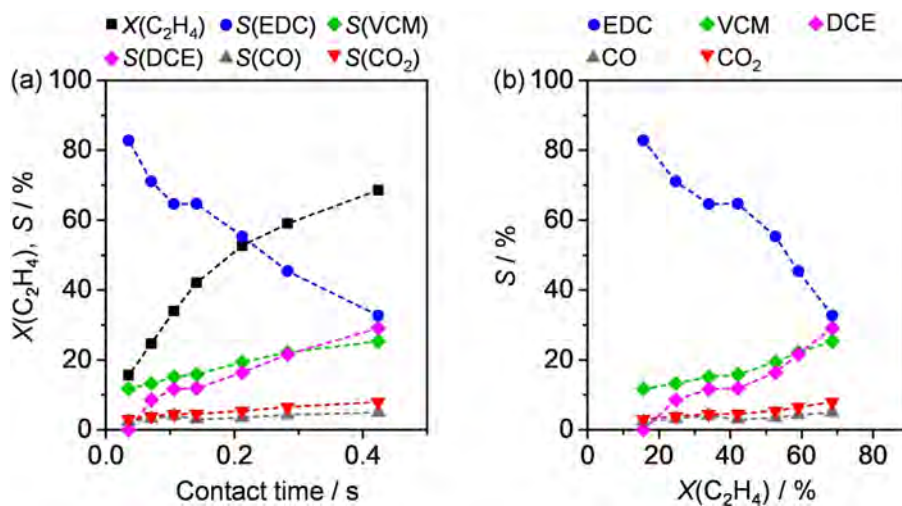
Figure S2. (a) Conversion (*X*) and selectivity (*S*) *versus* contact time and (b) selectivity *versus* conversion in ethylene oxychlorination on CeO$_2$-873. Conditions: *T* = 673 K, C$_2$H$_4$:HCl:O$_2$ = 3:4.8:3, F_{tot} = 100 cm^3 STP min^{-1}, *P* = 1 bar.

Molecule	Optimized geometries		
	Top	Side 1	Side 2
HCl			
C_2H_4			
C_2H_5Cl			
$C_2H_4Cl_2$			
C_2H_3Cl			
c-$C_2H_2Cl_2$			
t-$C_2H_2Cl_2$			
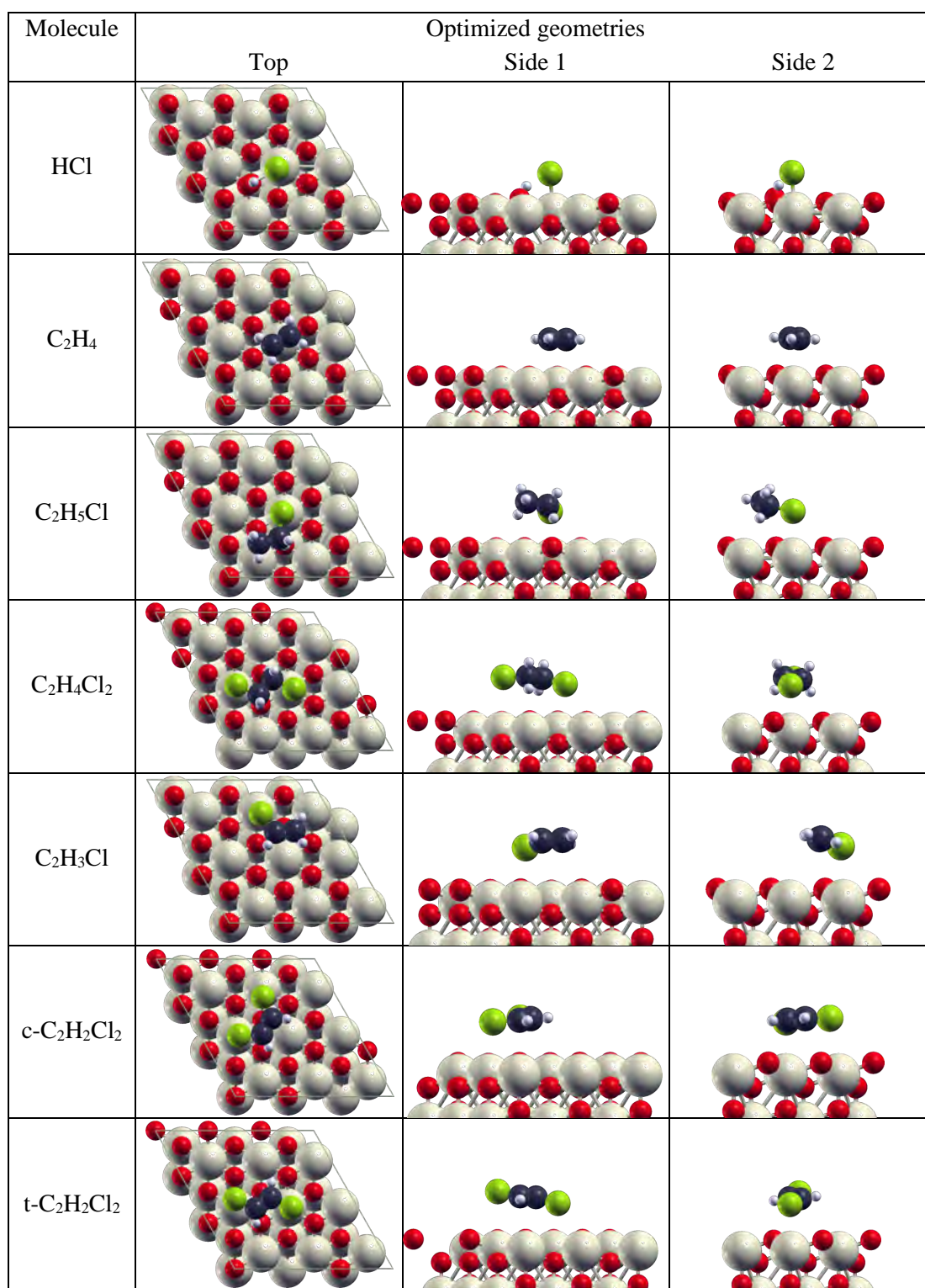
Figure S3. Optimized geometries of HCl and the investigated hydrocarbons adsorbed on a stoichiometric $CeO_2(111)$ surface. Color code: oxygen red, cerium yellow, carbon black, chlorine green and hydrogen white.

Molecule	Optimized geometries		
	Top	Side 1	Side 2
HCl			
C_2H_4			
C_2H_5Cl			
$C_2H_4Cl_2$			
C_2H_3Cl			
c-$C_2H_2Cl_2$			
t-$C_2H_2Cl_2$			
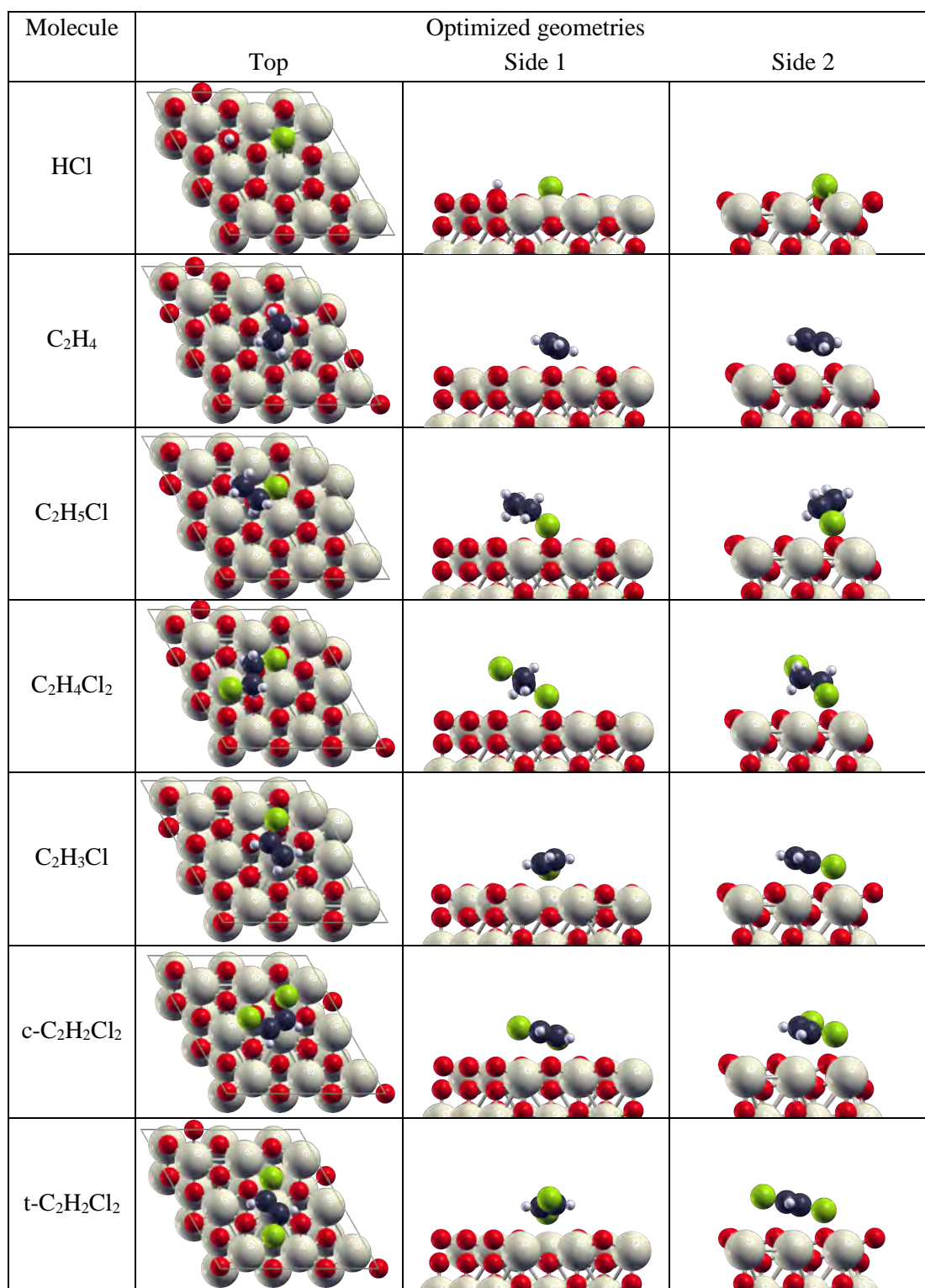
Figure S4. Optimized geometries of HCl and the investigated hydrocarbons, adsorbed on a defective $CeO_2(111)$ surface. Same color code as **Figure S3**.

Element. step. no.	Optimized geometries, top view		
	Initial	TS	Final
1			
2			
3			
4			
5			
6			
7			
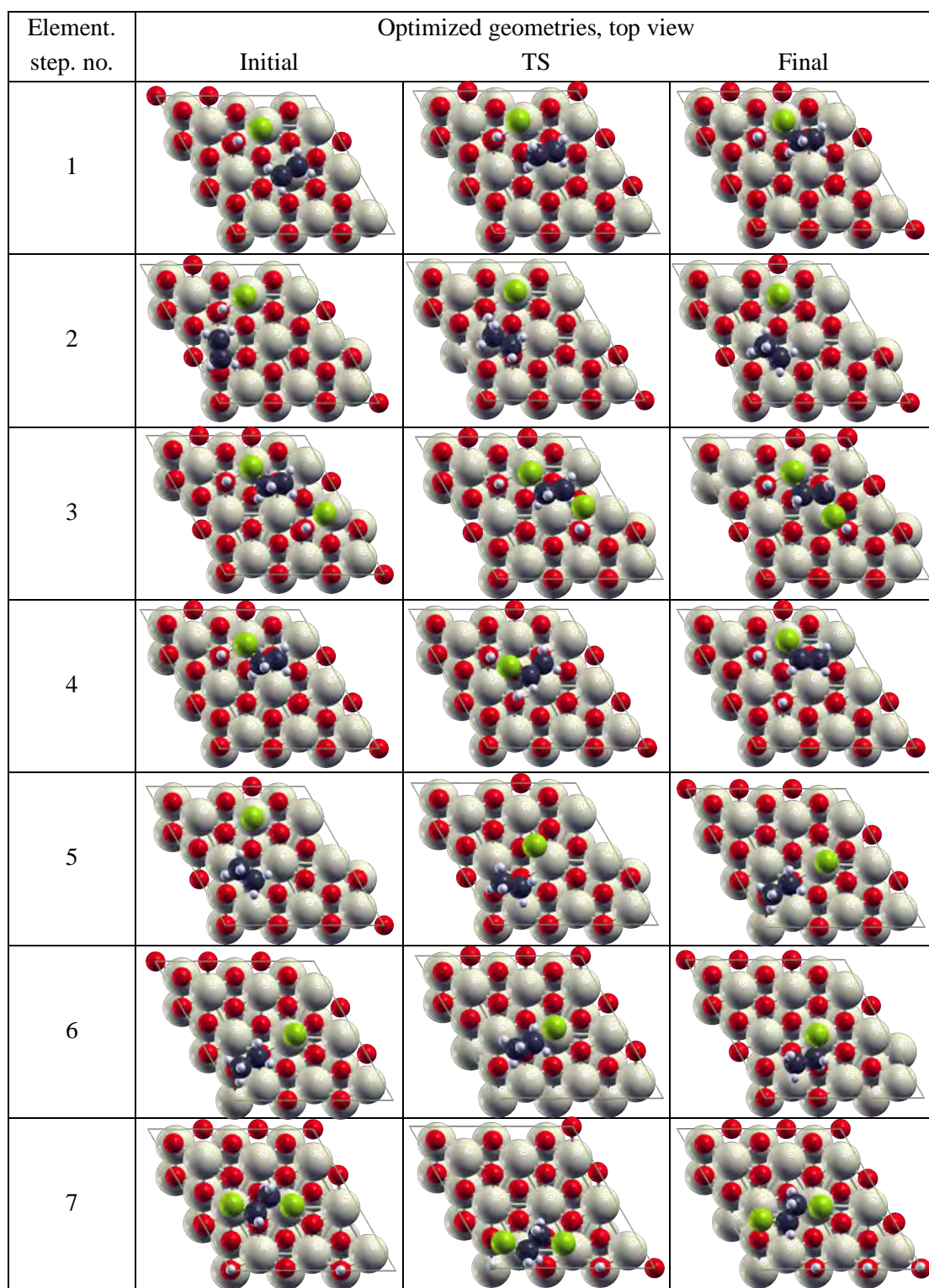
Figure S5. Top view of optimized initial, transition state (TS), and final geometries of the investigated elementary steps 1-7 on the stoichiometric $CeO_2(111)$ surface. Same color code as **Figure S3**.

Element. step no.	Optimized geometries, side view		
	Initial	TS	Final
1			
2			
3			
4			
5			
6			
7			
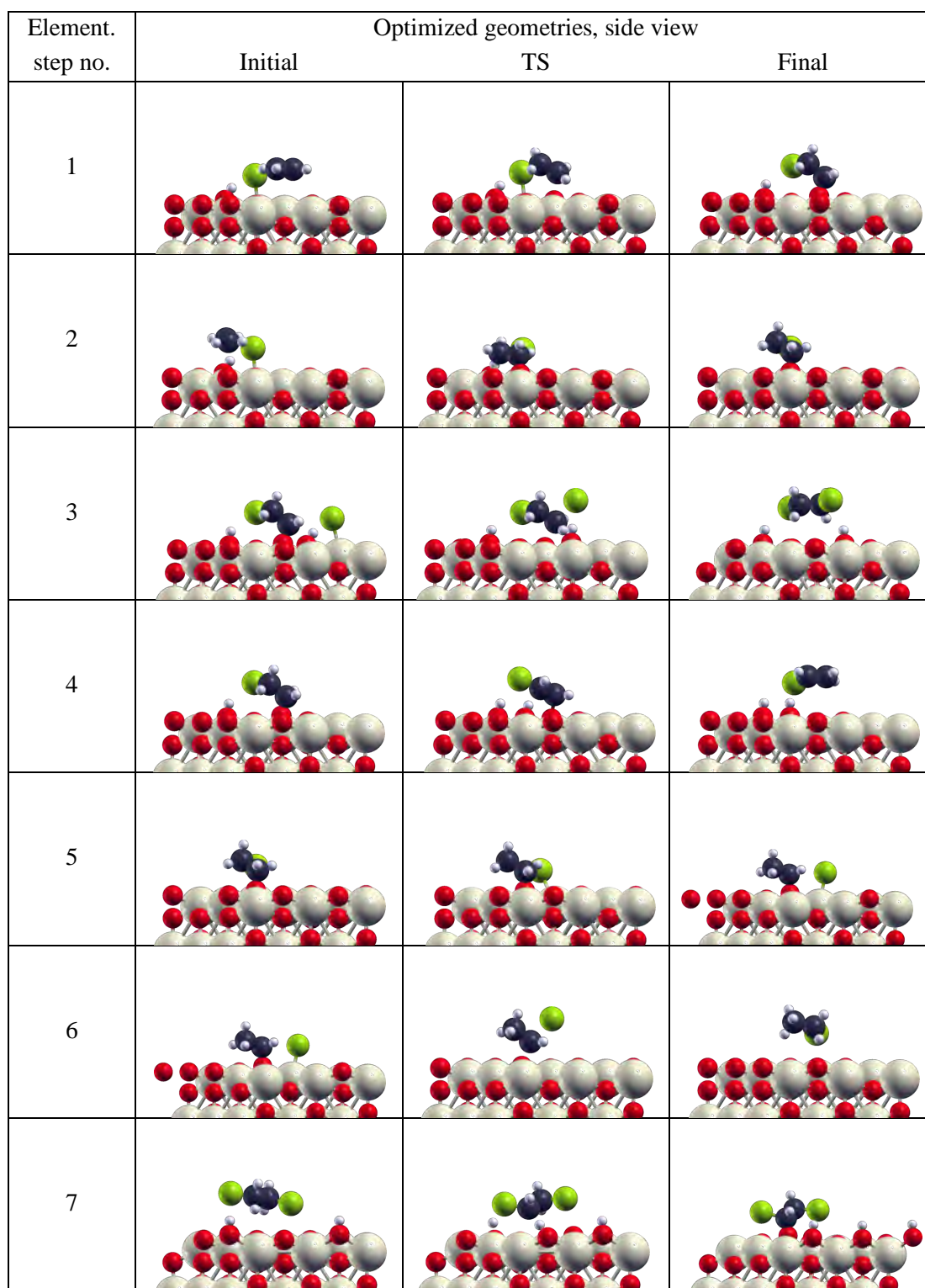
Figure S6. Side view of optimized initial, transition state (TS), and final geometries of the investigated elementary steps 1-7 on the stoichiometric $CeO_2(111)$ surface. Same color code as **Figure S3**.

Element. step no.	Optimized geometries, top view		
	Initial	TS	Final
7a			
9			
10			
11			
12			
13			
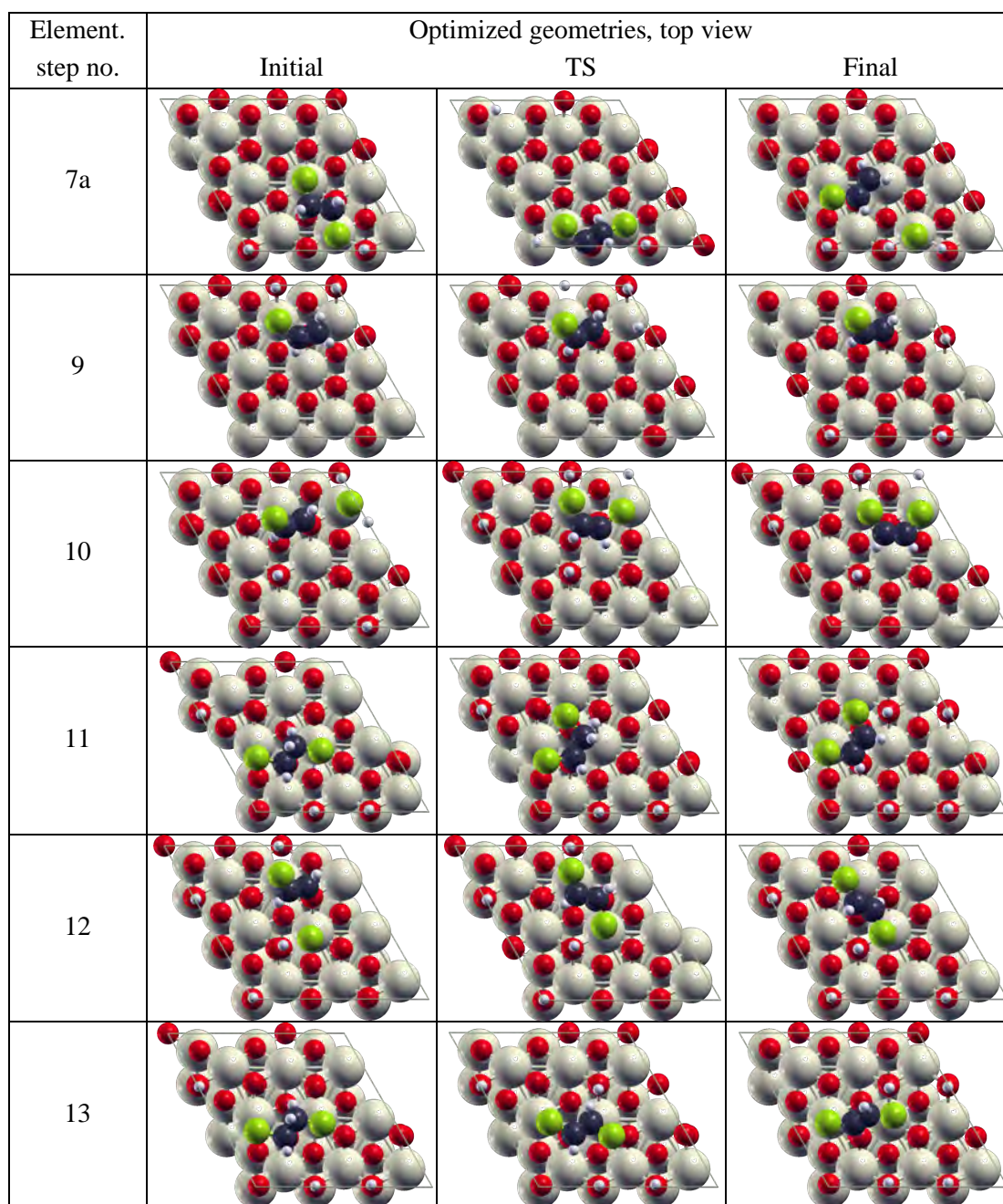
Figure S7. Top view of optimized initial, transition state (TS), and final geometries of the investigated elementary steps 7a-13 on the stoichiometric $CeO_2(111)$ surface. Same color code as **Figure S3**.
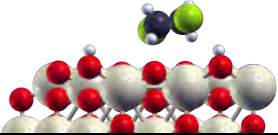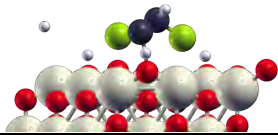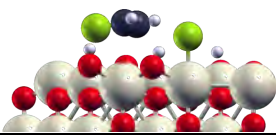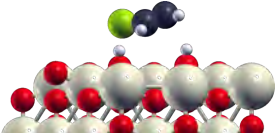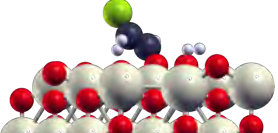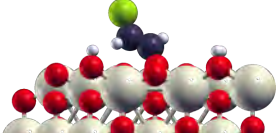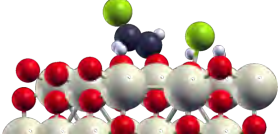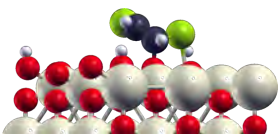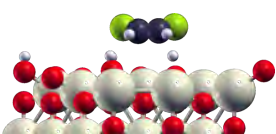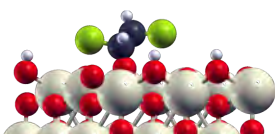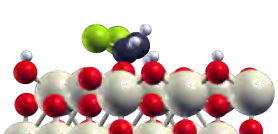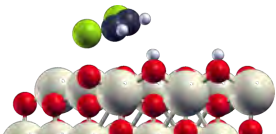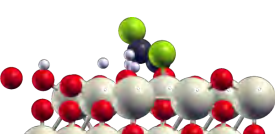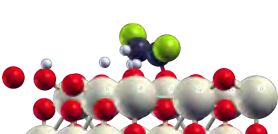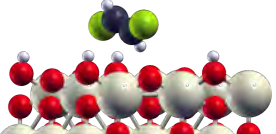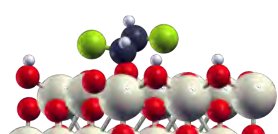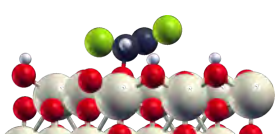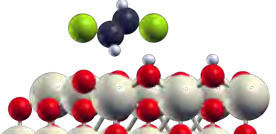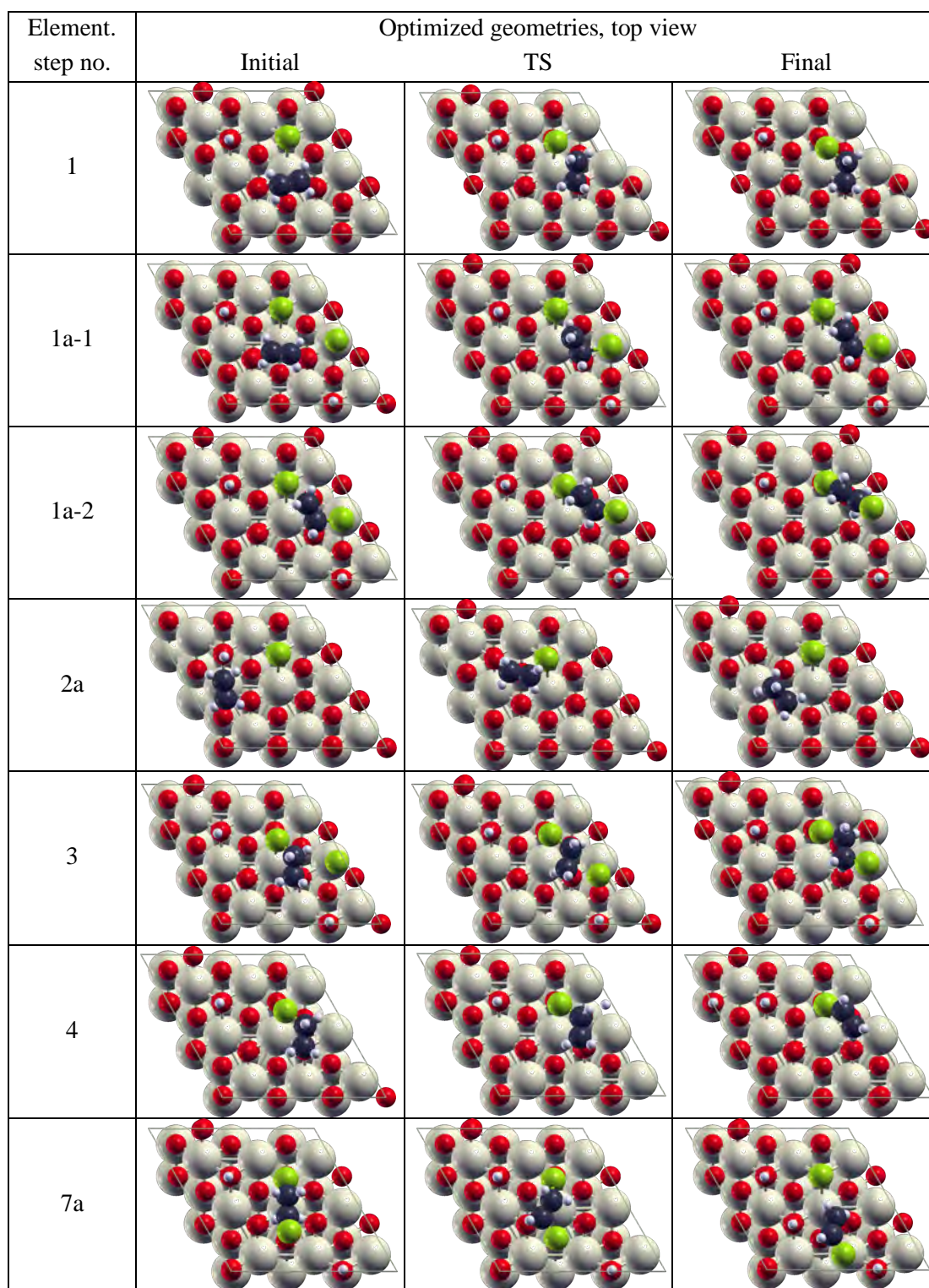
Element. step no.	Optimized geometries, side view		
	Initial	TS	Final
7a			
9			
10			
11			
12			
13			

Figure S8. Side view of optimized initial, transition state (TS), and final geometries of investigated elementary steps 7a-13 on the stoichiometric $CeO_2(111)$ surface. Same color code as **Figure S3**.

Element. step no.	Optimized geometries, top view		
	Initial	TS	Final
1			
1a-1			
1a-2			
2a			
3			
4			
7a			

Figure S9. Top view of optimized initial, transition state (TS), and final geometries of the investigated elementary steps 1-7a on the defective CeO_2(111) surface. Same color code as **Figure S3**.
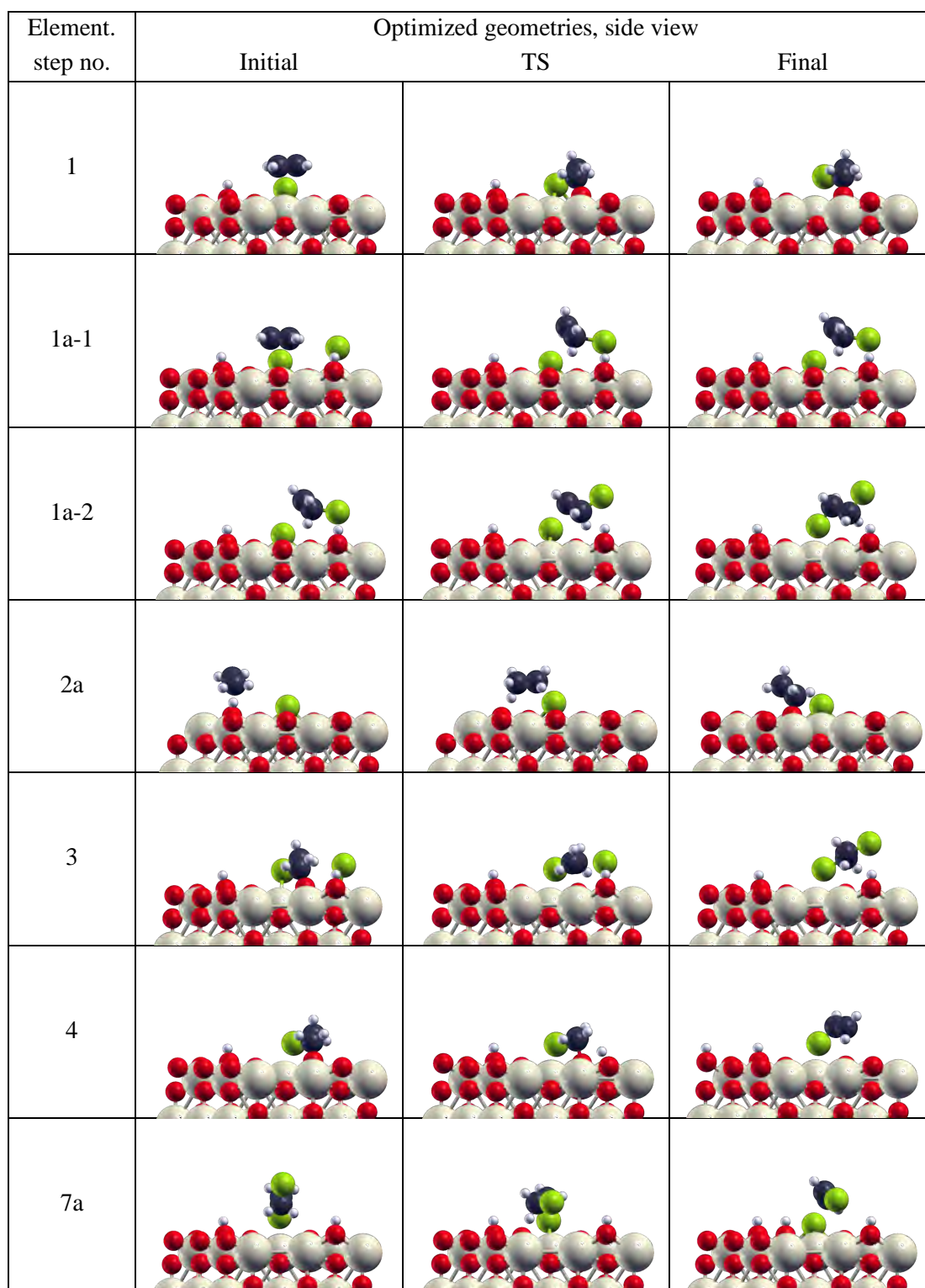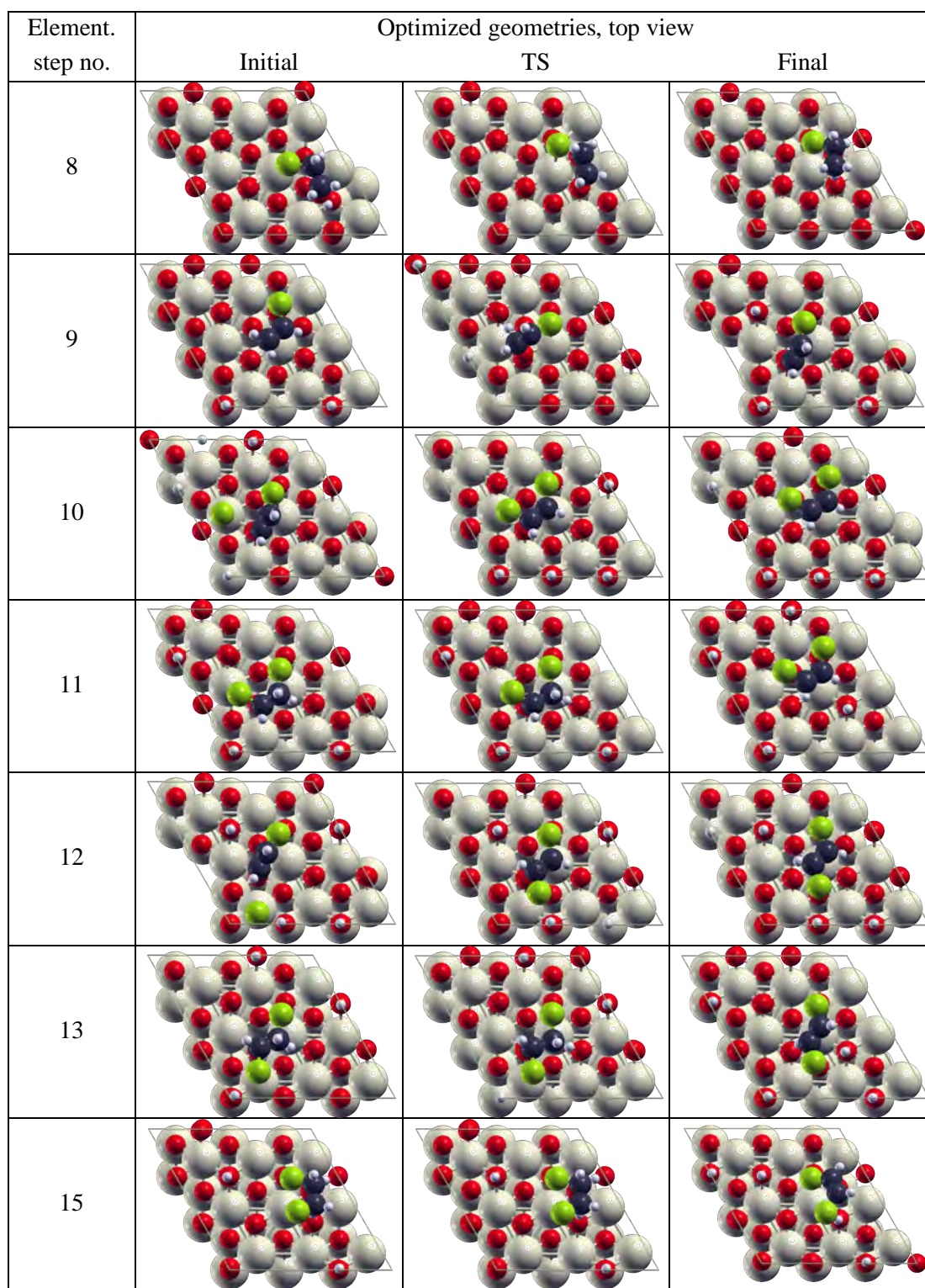
15

Element. step no.	Optimized geometries, side view		
	Initial	TS	Final
1			
1a-1			
1a-2			
2a			
3			
4			
7a			

Figure S10. Side view of optimized initial, transition state (TS), and final geometries of the investigated elementary steps 1-7a on the defective $CeO_2(111)$ surface. Same color code as **Figure S3**.

Element. step no.	Optimized geometries, top view		
	Initial	TS	Final
8			
9			
10			
11			
12			
13			
15			

Figure S11. Top view of optimized initial, transition state (TS), and final geometries of the investigated elementary steps 8-15 on the defective $CeO_2(111)$ surface. Same color code as **Figure S3**.

Element. step no.	Optimized geometries, side view		
	Initial	TS	Final
8			
9			
10			
11			
12			
13			
15			

Figure S12. Side view of optimized initial, transition state (TS), and final geometries of the investigated elementary steps 8-15 on the defective $CeO_2(111)$ surface. Same color code as **Figure S3**.
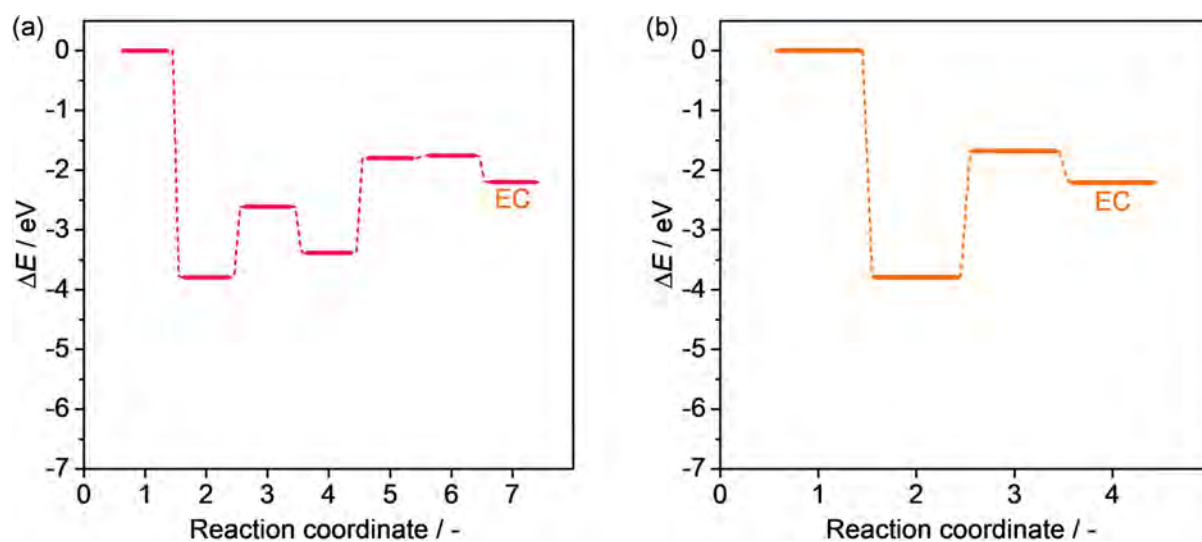
Figure S13. Reaction profiles for EC formation on a defective $CeO_2(111)$ surface through (a) steps 1 and 8 in **Figure 4** and **Table S2**, with the reaction coordinates described in **Table S3** and (b) steps 2a and 6 in **Figure 4** and **Table S2**, with the reaction coordinates described in **Table S4**.
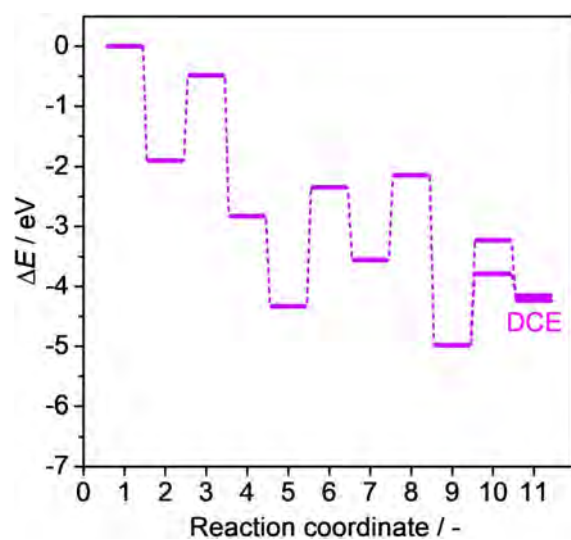
Figure S14. Reaction profile for DCE formation on a stoichiometric CeO₂(111) surface (steps 1, 3, 7, 11, and 13 in **Figure 4** and **Table S2**). The reaction coordinates are described in **Table S5**.
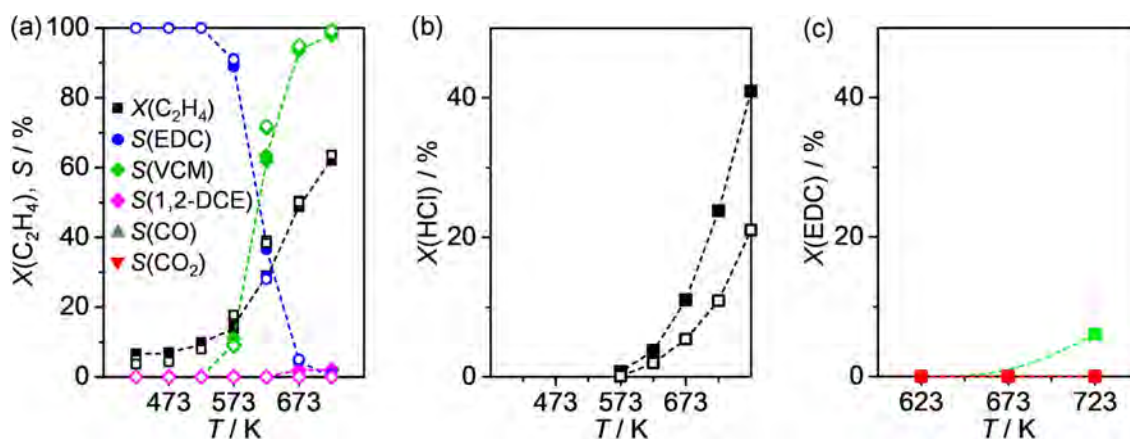
Figure S15. (a) Conversion (*X*) and selectivity (*S*) *versus* temperature in steady-state catalytic tests of ethylene chlorination with $Cl_2:C_2H_4:He = 2.4:3:94.6$ on quartz particles (solid symbols) and in an empty reactor (open symbols). (b) HCl conversion *versus* temperature in HCl oxidation on CeO_2-873 and CeO_2-NC with $HCl:O_2:He = 4.8:3:92.2$. (c) EDC conversion *versus* temperature in gas phase EDC dehydrochlorination with $EDC:He = 1.5:98.5$ or $EDC:O_2:He = 1.5:3:95.5$ (red), and $EDC:HCl:He = 1.5:4.8:93.7$ (green). Selectivity to VCM in all points: 100%. Other conditions: $W_{cat} = 0.5$ g, $F_{tot} = 100$ cm^3 STP min^{-1}, $P = 1$ bar.
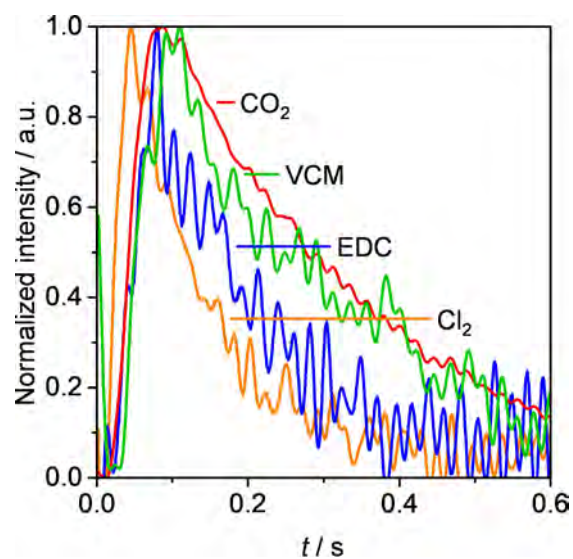
Figure S16. Normalized transient responses of CO_2, VCM, EDC, and Cl_2 upon simultaneous pulsing of HCl:Ar = 1:1 and C_2H_4:Ne = 1:1 in the TAP reactor at 773 K. The grey arrow indicates the time of the pulse of reactants.
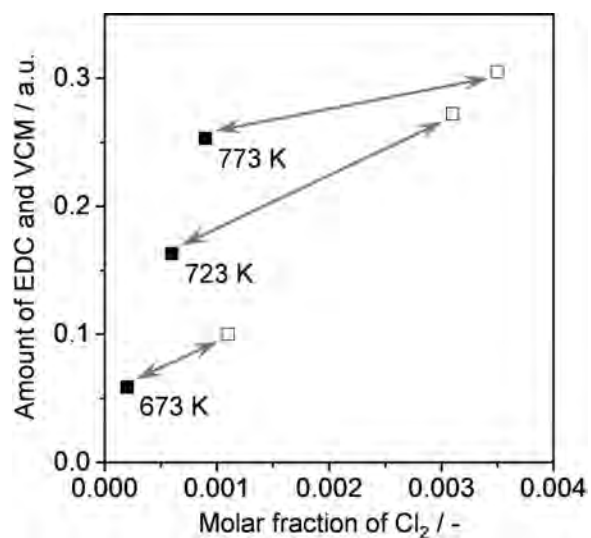
Figure S17. Amount of EDC and VCM (AMU 62) *versus* molar fraction of Cl_2 upon simultaneous pulsing of HCl:Ar = 1:1 and C_2H_4:O_2:Ne = 1:1:1 ($\square$) or HCl:Ar = 1:1 and C_2H_4:Ne = 1:1 ($\blacksquare$) at different temperatures in the TAP reactor.

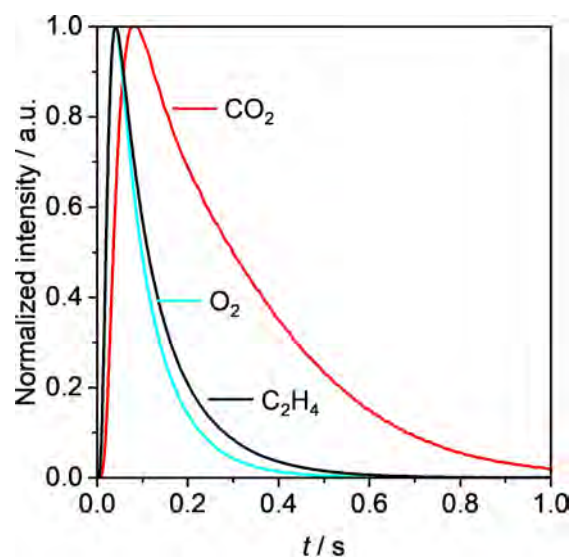**Figure S18.** Normalized transient responses of C_2H_4, O_2, and CO_2 upon pulsing of a mixture of $C_2H_4:O_2:Ne = 1:1:1$ in the TAP reactor at 773 K.